Icarus 260 (2015) 409–439

Contents lists available at ScienceDirect

Icarus

journal homepage: www.elsevier.com/locate/icarus

Gravitational spreading, bookshelf faulting, and tectonic evolution of the South Polar Terrain of Saturn's moon Enceladus

An Yin[a,*], Robert T. Pappalardo[b]

[a] Department of Earth, Planetary, and Space Sciences, University of California, Los Angeles, CA 90095-1567, USA
[b] M/S 321-560, Jet Propulsion Laboratory, California Institute of Technology, Pasadena, CA 91109, USA

ARTICLE INFO

Article history:
Received 26 December 2014
Revised 2 July 2015
Accepted 11 July 2015
Available online 7 August 2015

Keywords:
Enceladus
Ices, mechanical properties
Geological processes

ABSTRACT

Despite a decade of intense research the mechanical origin of the tiger-stripe fractures (TSF) and their geologic relationship to the hosting South Polar Terrain (SPT) of Enceladus remain poorly understood. Here we show via systematic photo-geological mapping that the semi-squared SPT is bounded by right-slip, left-slip, extensional, and contractional zones on its four edges. Discrete deformation along the edges in turn accommodates translation of the SPT as a single sheet with its transport direction parallel to the regional topographic gradient. This parallel relationship implies that the gradient of gravitational potential energy drove the SPT motion. In map view, internal deformation of the SPT is expressed by distributed right-slip shear parallel to the SPT transport direction. The broad right-slip shear across the whole SPT was facilitated by left-slip bookshelf faulting along the parallel TSF. We suggest that the flow-like tectonics, to the first approximation across the SPT on Enceladus, is best explained by the occurrence of a transient thermal event, which allowed the release of gravitational potential energy via lateral viscous flow within the thermally weakened ice shell.

1. Introduction

Enceladus, a small moon of Saturn with a diameter of ~500 km, is geologically active as expressed by eruption of gas and water–ice particles in plumes sourced from the parallel "tiger-stripe" fractures (TSF) in Enceladus' South Polar Terrain (SPT) (Porco et al., 2006, 2014) (Figs. 1A and 2A). The flux of the erupting plumes varies with time, possibly related to the diurnal variation of tidal stress that controls TSF opening and closing (Hurford et al., 2007; Hedman et al., 2013; Nimmo et al., 2014). The estimated surface age of the SPT is <0.5 Ma, which contrasts with 1–4 Ga surface ages of the surrounding terranes (Fig. 2) (Porco et al., 2006; Kirchoff and Schenk, 2009). Active geologic processes concentrated along the TSF are expressed by ejection of plumes (Porco et al., 2006; Spencer et al., 2009; Spencer and Nimmo, 2013). Because of this, understanding how the TSF were initiated and evolved is essential for determining the controlling mechanisms of active geologic processes and plume eruptions on Enceladus. In addition, as the SPT shares similarities in first-order structural style to that of the Trailing Hemisphere and Leading Hemisphere Terrains, which are both characterized by the development of circumferential belts (Crow-Willard and Pappalardo, 2015), establishing how the most dominant structures (i.e., TSF) in the SPT formed has important implications for global resurfacing processes of this icy moon.

Existing work attributes TSF initiation to formation of tensile cracks as a result of (1) the presence of a rectangular or elliptical thermal anomaly of an unspecified origin below the SPT that led to surface extension (Gioia et al., 2007), (2) icy-shell flexing induced by tidal stress (Nimmo et al., 2007), (3) true-polar wander of the satellite (Matsuyama and Nimmo, 2008), (4) non-synchronous rotation of Enceladus' ice shell above a global ocean relative to its solid rocky core (Patthoff and Kattenhorn, 2011), and (5) formation of a large rift basin (Walker et al., 2012). The subsequent kinematic evolution of the TSF after their initiation has been related to processes similar to those operated along divergent plate boundaries (Helfenstein et al., 2008) or strike-slip faulting with alternating senses of motion driven by cyclic tidal stress (Nimmo et al., 2007; Smith-Konter and Pappalardo, 2008). Extension along the proposed spreading centers at the TSF may be accommodated by deformation along the SPT margin (Helfenstein et al., 2006, 2008), which has been generally inferred to be entirely contractional (Porco et al., 2006; Spencer and

* Corresponding author.
E-mail addresses: yin@ess.ucla.edu, ayin54@gmail.com (A. Yin), Robert.Pappalardo@jpl.nasa.gov (R.T. Pappalardo).

http://dx.doi.org/10.1016/j.icarus.2015.07.017
0019-1035/

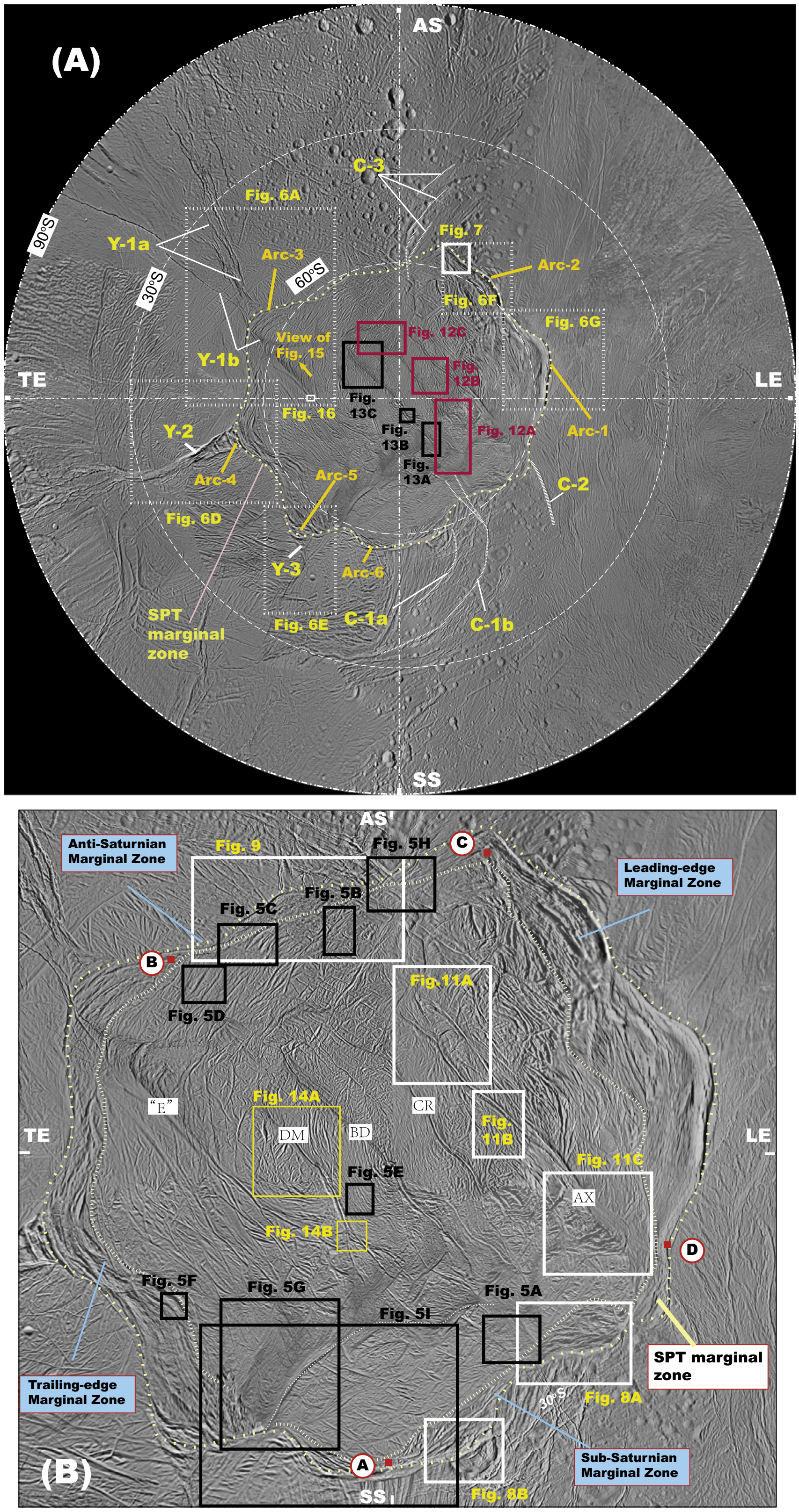

Fig. 1. (A) Image mosaic of the southern hemisphere of Enceladus collected by the Cassini orbiter's Imaging Science Subsystem (ISS) and constructed by the CICLOPS team (i.e., Cassini Imaging Team); the mosaic is in the south polar projection. This composite image serves as a context map for the South Polar Terrain (SPT) shown in (B) and Fig. 2A. Also shown are locations of figures mentioned in the text. Y-1 to Y-3 and C-1 to C-3 are Y-shaped and C-shaped fractures discussed in the text. (B) A close-up view of the SPT. Points A, B, C and D marked by red dots delimit the segmental ends of the SPT marginal zone (i.e., the sub-saturnian, anti-saturnian, leading-edge, and trailing-edge margins). Coordinate points SS, AS, LE, and TE are longitudinal directions from the south pole pointing toward the sub-saturnian (0° longitude), anti-saturnian (180°W), leading-edge (90°W), and trailing-edge (270°W) points on the equator of Enceladus, respectively. Abbreviations: AX, Alexandria fracture; CR, Cairo fracture; BD, Baghdad fracture; DM, Damascus fracture; "E", a newly designated fracture in this study. (For interpretation of the references to color in this figure legend, the reader is referred to the web version of this article.)

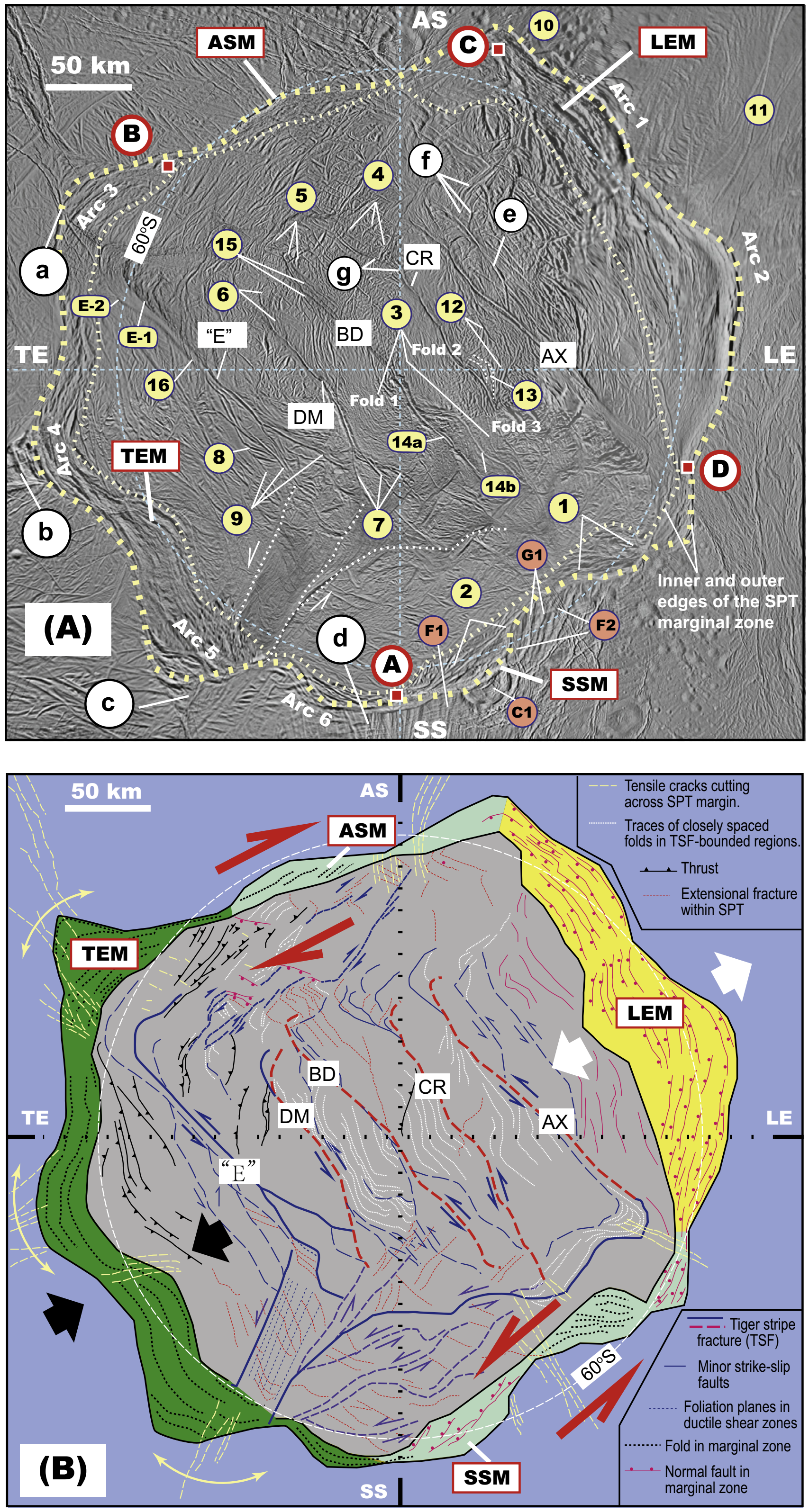

Fig. 2. (A) Cassini ISS image mosaic in south polar projection and (B) interpreted structural map of the South Polar Terrain (SPT). The designations in the red squares represent the four SPT marginal zones: AB = the trailing edge margin (TEM); BC = the anti-saturnian margin (SSM); CD = leading-edge margin (LEM); DA = sub-saturnian margin (SSM). Abbreviations for the five tiger-stripe fractures (TSF) are: AX for Alexandria fracture, CR for Cairo fracture, BD for Baghdad fracture, DM for Damascus fracture and "E" for a newly designated fracture in this study. Among the five TSF, only four (i.e., AX, CR, BD, and DM, shown in red dashed lines) are currently emitting plumes containing gas and water ice. Latitude 60°S (thin white dashed line) is shown on both figures. Numbers and lower-case letters with black circles refer to features discussed in detail in the text. Letters A, B, C, and D with red circles mark the ends of the sub-saturnian, anti-saturnian, leading-edge, and trailing-edge segments of the SPT marginal zone. (For interpretation of the references to color in this figure legend, the reader is referred to the web version of this article.)

Nimmo, 2013). An obvious issue with the above linkage between the marginal-zone deformation of the SPT and extension along the TSF is their kinematic incompatibility. That is, extension perpendicular to the TSF would be expected to have caused shortening only along the leading-edge margin (LEM) and the trailing-edge margin (TEM) parallel to the TSF (Fig. 2). In contrast, motion along the anti-saturnian-edge margin (ASM) and sub-saturnian-edge margin (SSM) should have been strike-slip (ASM and SSM in Fig. 2).

In this study, we address the above issue by conducting systematic photo-geologic mapping across the SPT. A key finding of this study is that the SPT has moved unidirectionally in the downslope direction of regional topography. Translation of the SPT was accompanied by map-view right-slip shear parallel to its transport direction and the shear deformation was accommodated by left-slip bookshelf faulting along the TSF. Our work suggests that gravitational spreading was a major driving force for the tectonic evolution of the SPT and TSF.

2. Regional geologic setting

Enceladus consists of three regions of deformation, namely the Leading Hemisphere Terrain (LHT), Trailing Hemisphere (THT), and South Polar Terrain (SPT) (Crow-Willard and Pappalardo, 2015). Each of these three terrains includes a circumferential belt that encloses one or more other structurally deformed units. The "semi-squared" SPT (Gioia et al., 2007) is a topographical depression 500–1500 m below its surrounding regions (Porco et al., 2006; Schenk and McKinnon, 2009). The region may be underlain by a local or global ocean (Collins and Goodman, 2007; Patthoff and Kattenhorn, 2011; Spencer and Nimmo, 2013; Iess et al., 2014; McKinnon, 2015; Thomas et al., submitted for publication). The cause for the formation and maintenance of a possible ocean below the SPT has been attributed to subsurface dissipation of tidal heating (Tobie et al., 2008), frictional heating along the TSF (Nimmo et al., 2007; Roberts and Nimmo, 2008), warm ice convection (Barr, 2008; O'Neill and Nimmo, 2010; Han et al., 2012), and combined steady and episodic tidal dissipative heating (Travis and Schubert, 2015). The TSF within the SPT (Porco et al., 2006) include Alexandria Sulcus (AX), Cairo Sulcus (CR), Baghdad Sulcus (BD), Damascus Sulcus (DM), and an informally named fracture referred to in this study as fracture zone "E" (Fig. 2). Although fracture zone "E" is similar in structural geometry to the other four tiger-stripe fracture zones, it was not examined in early studies, possibly due to a lack of erupting plumes (Porco et al., 2006, 2014).

The TSF zones are marked by ~100 m wide troughs that are bounded by raised double margins; each margin is ~2 km wide and ~0.5 km higher than the surrounding plains (Porco et al., 2006; Gioia et al., 2007; Spencer et al., 2009). Boulders of 20–50 m in size are composed of coarse-grained (~100 mm) ice crystals (mostly pure-water ice) and are littered along the TSF trough floors (Porco et al., 2006; Spencer et al., 2009; Martens et al., 2015). High thermal emission is concentrated along narrow zones (probably <10 m) within the TSF, expressed by high (~180–200 K) surface temperatures (Spencer et al., 2009, 2013; Goguen et al., 2013; Porco et al., 2014), which contrasts the average surface temperatures below 100 K in regions between tiger-stripe fractures (Spencer et al., 2009) and at 50–80 K outside the SPT (Howett et al., 2010). The high temperatures along the TSF are consistent with them being the sources of the erupting plumes (Porco et al., 2006, 2014). The areas bounded by the TSF are dominated by closely spaced (1–2 km) curvilinear ridges and troughs classified as the funiscular terrain by Barr and Preuss (2010) (Fig. 2A). The ridge-trough relief ranges from 10s to <200 m (Porco et al., 2006; Spencer et al., 2009).

3. Data and methods

3.1. Satellite-image and topographic data

The main data used in this study are satellite images obtained by the Imaging Science Subsystem (ISS) framing cameras carried by NASA's Cassini orbiter. These images are available publically from NASA's Planetary Data System (PDS). We also use digital topographic data derived from stereo images and photoclinometry by Schenk and McKinnon (2009) to aid our structural interpretations. The spatial resolutions of the satellite images used in this study vary from ~9 m to 110 m per pixel (http://photojournal.jpl.nasa.gov/target/Enceladus); the lowest resolution is for the entire south-polar image shown in Fig. 1A (see explanation of image PIA11679 by the Cassini Imaging Team at http://photojournal.jpl.nasa.gov/catalog/PIA11679). The spatial resolutions of the topographic data are 200–950 m in the horizontal direction and 50–140 m in the vertical direction according to Schenk and McKinnon (2009).

3.2. Methods of geologic mapping and kinematic analysis

The main focus of this study is to map the spatial distribution of major structures, their mutual cross-cutting relationships, and features indicative of kinematic development of the mapped structures. This effort results in a structural map of the SPT (Fig. 2B) that contrasts with most planetary geologic maps that display mostly geomorphic features with little or no emphasis on determining the kinematics of major faults (e.g., Figueredo and Greeley, 2000; cf., Schultz et al., 2010; Yin, 2012a, 2012b; Crow-Willard and Pappalardo, 2015). We determine structural kinematics using minor structures within and next to major deformation zones and minor structures that terminate major structures.

We define termination structures as those that occur at the tips of a long fault/shear zone (10s km). The terminations may have different orientations from the trend of the main structures (for example, orthogonally oriented extensional or contractional termination structures at the ends of major strike-slip faults) (Woodcock and Fischer, 1986; Peltzer and Tapponnier, 1988; Burchfiel et al., 1989; Yin et al., 2002). The termination structures could also be expressed by fault bifurcation due to progressive decrease in the magnitude of strain accommodated by faults. For example, strike-slip faults could die out via the development of horsetail structures (Sylvester, 1988) as exemplified at the western end of the active Kunlun fault in central Tibet (Yin, 2000; Yin et al., 2008; Taylor and Yin, 2009). Finally, termination structures could be expressed as zones of *en echelon* folds, faults, extensional cracks, and tail cracks (e.g., Segall and Pollard, 1983).

Dip-slip fault/shear zones may die out along strike due to diminishing slip along fault strike. However, they could also terminate at strike-slip faults oriented at high angles to the main fault trend (Fig. 3A and B) (e.g., Boyer and Elliott, 1982; Lister et al., 1986; Taylor et al., 2003; Yin and Taylor, 2011). For the latter situation, the kinematics of strike-slip termination structures provides important information for the sense of slip along the linked dip-slip faults. Secondary structures associated with a dip-slip fault/shear zone should be parallel to the main faults and their spacing and the accommodated magnitude of strain should decrease away from the main faults/shear zones (e.g., Boyer and Elliott, 1982; Lister and Davis, 1989; Kim and Sanderson, 2006) (Fig. 3A and B). Secondary structures may also display *en echelon*, drag-fold, horse-tail/tail cracks, and duplex patterns (e.g., Segall and Pollard, 1983; Woodcock and Fischer, 1986; Swanson, 1988; Willemse et al., 1997; Cowgill et al., 2000, 2004a, 2004b; Kattenhorn, 2004) (Fig. 3C–E).

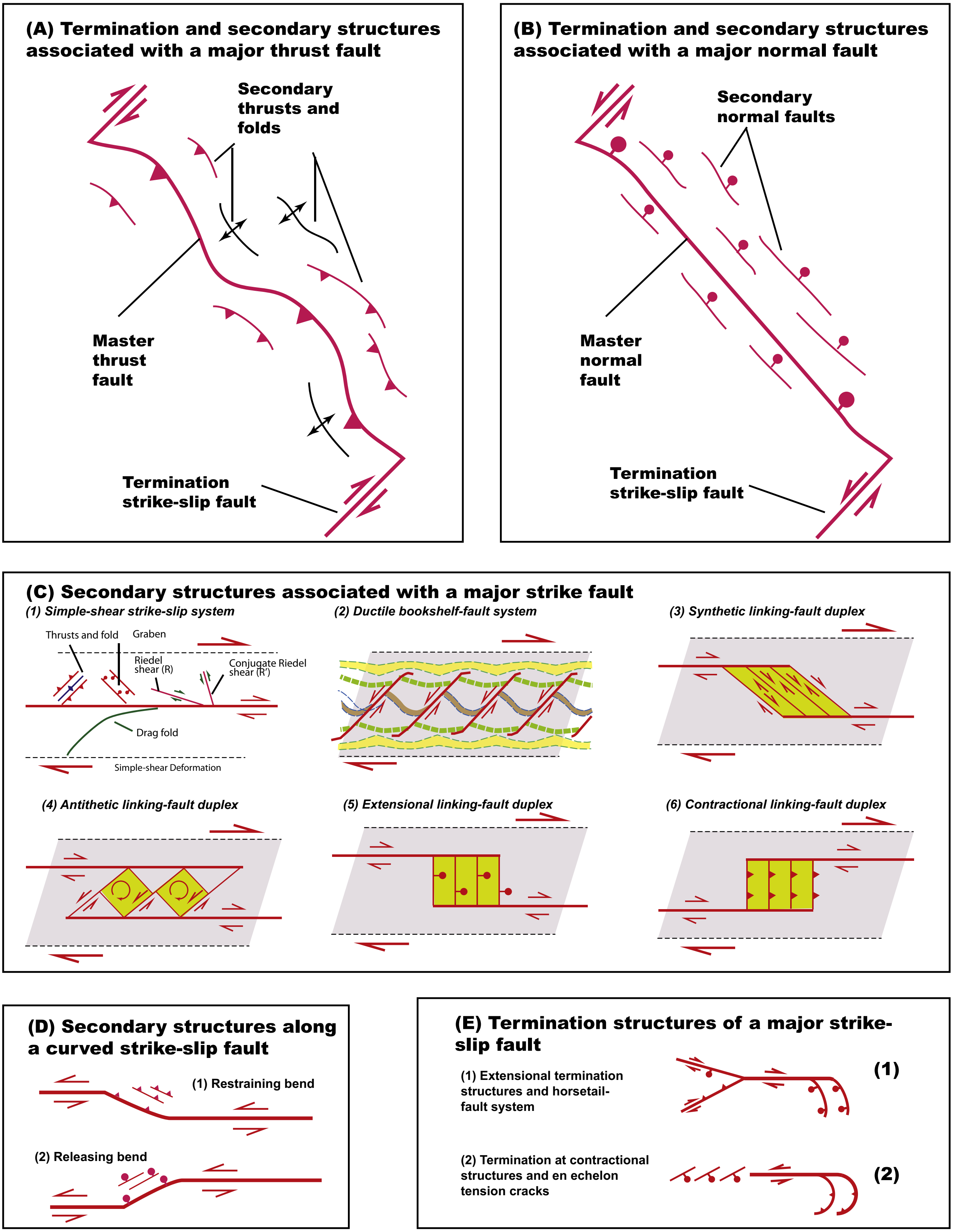

Fig. 3. Schematic showing fault termination and associated secondary structures. (A and B) show termination and secondary structures associated with a major thrust and normal fault. (C–E) show secondary structures associated with a major strike-slip fault system. Small triangles are on the hanging walls of thrust faults and small circles are on the hanging walls of normal faults.

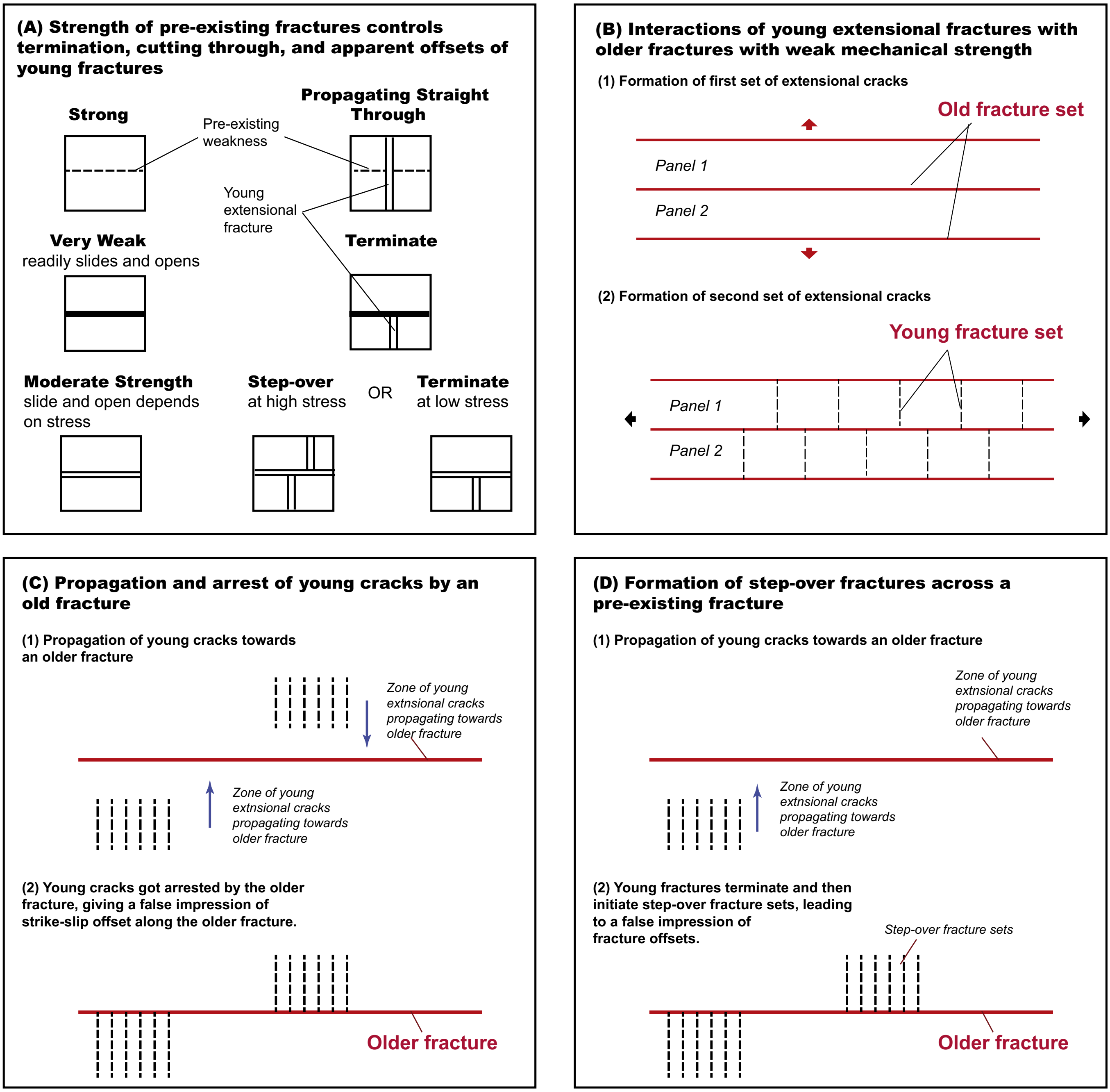

Fig. 4. Termination of younger propagating extensional fractures at older pre-existing surfaces can lead to a false impression that the younger systematic fractures are offset by the older surfaces (Cooke and Underwood, 2001). (A) Whether young fractures propagate straight through, jump across with apparent offsets, or terminate at an older pre-existing fracture depends on the frictional strength of the pre-existing weakness (Cooke and Underwood, 2001). For an older fracture with a high frictional strength (essentially locked as the coefficient of friction is required to be much higher than the internal coefficient of friction at a value of >0.65), the young crack is expected to propagate through the pre-existing fracture plane. However, for an older fracture with a moderate strength (i.e., coefficient of friction is ∼0.65), the young fractures either terminate or initiate a step-over fracture on the other side of the older fracture. Finally, for an older fracture with a very low frictional strength (≪0.65), the propagating young fractures are expected to terminate at the older fracture surfaces. (B) Young extensional fractures form in panels bounded by older fractures. Although they have the same spacing, the independent development of the young fracture sets in different panels leads to a systematic apparent offset of the fractures along the older fractures. Using this apparent offset to determine the lateral motion along the older fractures would lead to both incorrect interpretation of the timing of the fracture formation sequence and the kinematic nature of the older fractures. (C) Propagation of two zones of young extensional fractures toward an older fracture. Their termination due to crack-tip arresting at the older fracture leads to an apparent offset of a fracture zone. Again, using the apparent offsets along the older fracture to establish its lateral displacement can lead to incorrect assignment of fracture-formation sequence and fracture kinematics. (D) Formation of step-over fractures across an older fracture surface can also lead to apparent offset along the older fracture surface.

To be consistent in our mapping, we define secondary structures as those that occur adjacent to major faults/shear zones; their spatial relationships should be indicative of coeval development but the magnitude of deformation should be significantly smaller than that accommodated by the main faults/shear zones. Also, the density of secondary structures should decrease away from the main structures, indicating a decrease in strain magnitude (e.g., Yin and Kelty, 1991; Kim and Sanderson, 2006).

It is important to note that our structural analysis on fault kinematics and age relationships does not rely on apparent offsets of

Table 1
Criteria for identifying various types of structures.

	Tension cracks	Normal faults	Thrust faults	Circular folds	Box folds	Strike-slip faults
Ridge morphology in cross section view	Commonly not associated with ridge formation	(a) Sharp ridge crest; (b) one side of the ridge displays high-angle planar scarps	(a) Irregular ridge crests; (b) symmetric ridge slopes with the steep side above fault traces	(a) Semi-circular ridge crest in cross section view; (b) smooth and symmetric ridge slopes but without planar scarps	(a) Flat ridge tops; (b) steep to vertical ridge flanks defining vertical fold limbs	Sharp ridge crest and nearly vertical scarps when exposed
Trough morphology in cross section view	Steep walls bounded by high-angle fractures	Depression correlates with the extent of the bounding faults	Irregular shaped basins induced by thrust loading in the footwalls	Troughs are synclinal folds with circular cross section geometry	Steep walls bounded by draped limbs from flat fold top. This differs from extensional cracks where bounding normal faults truncate footwall layers	At local releasing bends and pull apart basins with morphology similar to that related to normal faults
Scarp shape and fault-induced depression geometry	Relatively constant height for scarps. Constant width of depression	Scarp height decreases laterally. Induced trough width decreases toward fault tips	Variable scarp heights and trough width	No sharp scarps; synclinal depressions do not have flat floors common for graben basins	Sharp scarps, flat trough floors, and constant trough width	Variable scarp heights and facing directions depending on local fault dip and local strike relative to slip direction
Map-view geometry of mapped structures	Straight traces and parallel sets with even spacing	Relatively straight fault trace	Highly curved, wavy fault traces. More discontinuous than fold traces	Both straight and curvilinear traces	Steep walls bounded by high-angle fractures	Generally straight traces; en echelon pattern when occur in groups
Termination structures	Cracks die out along strike	Normal faults could be linked with strike-slip faults or die out along strike	Thrusts could be linked with strike-slip faults at fault tips or die out along strike	(a) Folds and thrusts can occur in the same belt (b) Folds can terminate at strike-slip faults	(a) Folds and thrusts can occur in the same belt (b) Folds can terminate at strike-slip faults	Oblique or en echelon thrusts, folds, normal faults, and strike-slip faults can all occur
Secondary structures	None	Parallel normal faults near main fault	Parallel thrusts and folds near main fault	Parallel folds	Parallel folds	En echelon folds, faults, and tension cracks

extensional fractures, as this method may yield ambiguous results when corroborative observations are not available. Cooke and Underwood (2001) show that young propagating tensile fractures can either cut across older fractures if they have high frictional strength or terminate at the older fractures if they have low frictional strength (Fig. 4A). In the case of young fractures terminating at older fractures, using this apparent offset to infer lateral motion would lead to two erroneous conclusions: (1) the older fractures would appear to postdate the younger fractures and (2) the older fractures would also appear to be strike-slip faults with consistent lateral offsets of the younger fractures that in fact terminate rather than are offset by the pre-existing fractures (Fig. 4B–D).

3.3. Structural identification and kinematic interpretations

Erosion and deposition may alter the landforms generated by ice shell deformation on Enceladus. The main processes of erosion include sublimation, space weathering, and mass wasting. Data from the Magnetospheric Imaging Instrument on the Cassini spacecraft indicate that space weathering does not play a significant role in modifying the surfaces of Saturn's inner satellites (e.g., Paranicas et al., 2012). Sublimation of an icy satellite surface below 100 K is expected to have little effect on altering surface morphology over the age of the Solar System (Sieveka and Johnson, 1982). In the SPT, the temperatures along the TSF can be as high as 180–200 K during eruption of vapor jets. Under such temperatures, the sublimation rate could be as high as 1 m/h (Goguen et al., 2013). However, such high temperatures are restricted to meter-scale zones (Goguen et al., 2013) and decrease rapidly within a few hundred meters away surface temperatures, which are at or below 100 K (e.g., Spencer et al., 2009; Goguen et al., 2013). Extrapolating the relationship between ice vaporization and temperature constructed by Ingersoll and Pankine (2010, p. 596) and used by Goguen et al. (2013; see their Fig. 5a), sublimating a 1 m thick ice layer at 100 K on Enceladus' surface would have taken >1 Ga. As the age of the SPT is only a few million years old (Porco et al., 2006), the amount of erosion since the formation of the SPT is only a few mm. Mass wasting is closely associated with the presence of down-slope transported debris; it only affects the landforms locally and can be readily recognized by carefully examining the high-resolution satellite images.

Erupted ice grains from the TSF may fall back and then deposit on the surface of Enceladus (Schenk et al., 2011a, 2011b). Based on the results of first-principle calculations, the size of the particles formed by condensation growth via heterogeneous nucleation from the eruption vents is proportional to vent size; only vents several tens to hundreds of meters in size are capable of producing the micron-sized grains (Yeoh et al., 2015). Schenk et al. (2011a, 2011b) show that the fine-grained particles may have draped over the surface of Enceladus, detectable in the highest-resolution images (~10 m/pixel); the fine-grained sediments obscure the fine textures but not the overall structures of the landform (see Fig. 2 of Schenk et al., 2011a, 2011b).

Because erosion and deposition are negligible, we use the criteria of neo-tectonic mapping on Earth to identify tectonically induced structures (Yeats et al., 1997; Burbank and Anderson, 2011; cf. Pappalardo and Greeley, 1995). This approach allows us to map and infer the following structures: (1) closely spaced tension-crack/extensional-fracture zones, (2) normal faults and fault-bounded grabens, (3) thrusts, (4) folds, and (5) discrete strike-slip faults and distributed ductile shear zones (Table 1).

Lighting directions and angles are important for detecting tectonically induced topographic features (Watters et al., 2010). For perfectly linear topographic features, they are best imaged when the trend of the lighting direction is perpendicular to and the inclination of the lighting direction is at a low angle to the surface of the interested features. However, the features are poorly displayed when the trend of the lighting direction is parallel to the long dimension of the feature and the inclination angle of the lighting direction is at a high angle to the long dimension surface of the features. For all the cases we have analyzed, the topographic features are highly nonlinear and thus even segments of the features are obscured by the effect of parallel lighting, the overall shading of the features is sufficient for deducting their geometry and morphologic characteristics.

Tensile cracks and grabens. Tensile cracks and grabens are the most readily recognizable features, identified by the following characteristics: (a) narrow depressions with linear traces, (b) bounded by fault-controlled and nearly vertical walls, and (c) parallel fractures with even spacing (Table 1). Some tensile cracks display *en echelon* patterns in strike-slip shear zones.

Normal faults. Normal, thrust, and strike-slip faults can be distinguished by their ridge-crest and ridge-slope morphology (Table 1). A normal fault displays an inclined planar scarp. This contrasts with a strike-slip fault, which displays a vertical planar scarp and a thrust fault does not produce a planar scarp.

Thrusts. Thrusts commonly create asymmetric topography: the ridge flanks directly above the fault traces commonly have steeper slopes (e.g., Walker et al., 2003) (Table 1). Three key features distinguish thrusts from normal faults: (1) curvilinear ridge traces due to their low dip angles, (2) a lack of planar scarp, and (3) spatial association with parallel folds (e.g., Jackson et al., 1982, 1988).

Strike-slip faults. Ideally, planar strike-slip faults should have straight fault traces and vertical orientation near the stress-free surface (Anderson, 1942). However, if the wall rock is not rigid but instead deformable, the trace of a strike-slip fault may be curvilinear but not affected by local topography due to its vertical orientation. Diagnostic features of a strike-slip fault zone include the presence of *en echelon* folds, *en echelon* extensional fractures, Riedel (R) and conjugate Riedel (R′) shear zones, and oroclinal drag folds aside the main strike-slip fault/shear zones (Table 1) (Sylvester, 1988).

Folds. Two types of folds are relevant to the study area: (1) folds with a circular cross-sectional geometry and well-preserved sub-horizontal fold-hinge zones (i.e., they are expressed as rounded-top ridges flanked by relatively symmetric and equal-length flanking slopes) (Table 1), and (2) folds whose hinge zones are partially refolded, displaying as apparent plunging geometry (see an example described in detail below).

Ductile shear zones. Ductile shear zones typically display sharp boundaries that truncate structures outside the shear zones and contain parallel linear ridges and troughs within the shear zones (Table 1). The parallel ridges and troughs, typically closely and evenly spaced, are expressions of shear-zone foliation planes. In addition, *en echelon* tension cracks similar to obliquely orientated crevasses in the margins of flowing glaciers (Nye, 1952; Paterson and Cuffey, 1994) are also present. Finally, oroclinal drag folds may be present next to or inside the ductile shear zones. The high temperatures (180–200 K) related to eruption of vapor and ice-grain jets may last for days or even months, responsible for widening erupting fissures and may also be conducive for local development of ductile shear zones along the TSF zones and ductile drag folds.

Unrelated structures. In any mapping, there may be some structures that appear to be correlated in style and morphology, but their formation is unrelated. There are many examples of such cases in our mapping area; structures in the SPT are relics of older surfaces and structures and may or may not be modified by later deformation related to the development of the SPT. We refer to these relic features as pre-SPT structures and their effects are carefully removed when analyzing the kinematics of structures in the SPT.

3.4. Examples of mapped structures

Below we use a few examples to illustrate our mapping procedure for creating the tectonic map shown in Fig. 2B. The locations of the illustrating images are shown in Fig. 1B. The image in Fig. 5A shows two sets of closely spaced grooves interpreted as extensional cracks. This interpretation is mainly based on the observation that there are no raised margins along the grooves, consistent with formation of extensional fissures over an originally flat surface. The older set of interpreted tension cracks have curved traces, which may have resulted from distortion from later deformation or a stress field characterized by spatially varying directions of the principal stresses. The younger set of tensile cracks displays a similar morphology but has straighter traces.

Fig. 5B shows minor right-slip faults associated with inferred small drag folds. The interpreted drag folds are defined by dramatically curved troughs; the bends are too sharp to be explained by stress fields with varying directions of principal stresses over such a small area. We thus interpret the curvilinear troughs as oroclinal folds against the interpreted right-slip faults.

Fig. 5C shows an interpreted normal fault scarp that truncates early structures expressed as ridges and grooves oriented nearly perpendicular to the interpreted scarp. The fault scarp within the SPT lies against the anti-saturnian margin (ASM) and its oblique orientation to the margin is consistent with right-slip shear along the ASM. Also shown in the figure are a high-topography and high-relief region in the footwall and a low-topography and low-relief region in the hanging wall of the interpreted normal fault. Offset ridges by the normal fault scarp can be recognized across the fault, but the matching ridges offset by the fault on the hanging-wall side display much more subdued topography and relief. The lack of relief in the hanging wall may be explained by ice-shell stretching during normal faulting. Fig. 5C also shows that the normal fault scarp is truncated by the sub-saturnian marginal zone (ASM), which is defined by a series of sub-parallel ridges and troughs. As the normal-fault scarp has no counterpart on the other side of the ASM (i.e., outside of the SPT), we interpret its development to be coeval with shear deformation along the marginal zone. The lack of normal faults outside the SPT directly against the ASM boundary can be explained by its thicker ice shell as indicated by the higher topography (Schenk and McKinnon, 2009). The oblique orientation of the normal fault would in turn require the ASM to be a right-slip structure. Obliquely oriented, irregular ridges are present in the sub-saturnian marginal zone (Fig. 5C). Width changes along individual ridges in the shear zone, whereas the average width of the ridges also varies from one another (Fig. 5C). As the edges of the ridges are highly irregular, the ridge topography is unlikely to be generated by faulting. As erosion is negligible on Enceladus, the ridges in the shear zone are interpreted to have been generated by folding. The oblique orientation of the interpreted folds is consistent with right-slip shear along the ASM.

Fig. 5D displays ridges with asymmetric ridge flanks: one side is long and gentle and the other side is short and steep. The height and width of the ridges change along their trend, but the edges of the steep flanks are rather straight, suggesting a tectonic origin. As the ridge crests are higher than the surrounding regions, their formation must have been related to contractional deformation. Based on the above arguments, we interpret the asymmetric ridges as morphologic expressions of thrusts and/or thrust-induced folds (i.e., fault-propagation folds or fault-bend folds).

Fig. 5E shows rounded-top and symmetric-flank ridges. The ridge height, width, and spacing are rather constant in general. This type of ridge morphology was interpreted as folds by Barr and Preuss (2010). We agree with their classification of these structures as folds but disagree with their interpreted fold origin. In our interpretation, the closely spaced folds formed during the

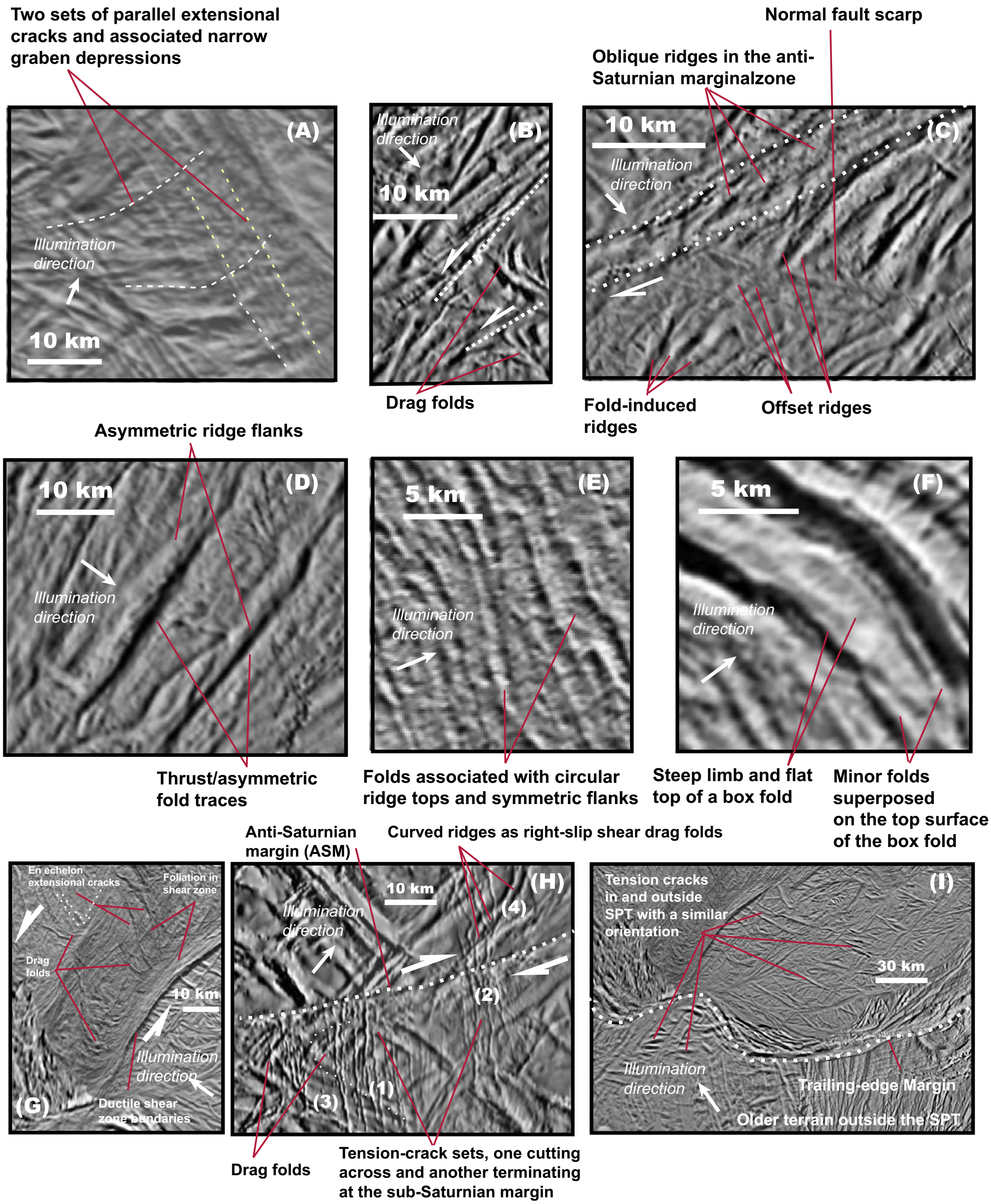

Fig. 5. Examples of interpreted structures and the corresponding morphology. See Fig. 1B for locations. The resolution of all the figures is 110 m/pixel. The top, bottom, left, and right sides of all the figures point toward the anti-saturnian, sub-saturnian, leading-edge, and trailing-edge directions. (A) Two sets of parallel extensional cracks and associated narrow depressions interpreted as grabens. (B) Inferred oroclinal folds induced by right-slip shear deformation. (C) A normal fault scarp that truncates earlier structures expressed as ridges and grooves, and which separates a high-topography region in the footwall from a low depression in the hanging wall. (D) Ridges with asymmetric flanking slopes: one is long and gently sloping, whereas the other is short and steeply sloping. The ridges are interpreted thrust induced features. (E) Rounded ridge tops with symmetric ridge flanking slope are interpreted as the morphological expression of folds. (F) A possible example of a box fold with a flat top and nearly vertical fold limbs. (G) An example of a ductile shear zone that consists of *en echelon* extensional fractures oriented obliquely to the edges of the shear zone. The closely spaced ridges parallel to the shear-zone margins are interpreted as shear foliation planes. Drag folds are inferred directly outside the interpreted strike-slip shear zone. (H) Structures near the sub-saturnian margin (SSM) of the South Polar Terrain (SPT). One set of extensional fractures (site 1) trends in the SSM direction and cuts across a curvilinear ridge-groove zone (site 3) that are interpreted as drag folds associated with left-slip motion across the SSM. The same set of extensional fractures (on the lower left side of the image) terminates at the SSM, suggesting that its formation occurred either during or after motion on the SSM. Drag folds expressed by curved ridges and troughs are also present at site 3. Another set of tension cracks at site 2, and trending parallel to the set at site 1, cuts across the SSM. (I) Extensional fractures trending in the same direction, and displaying similar length and morphology, are present both within and outside the SPT.

earliest stage of the SPT formation when its ice-shell was thin (see details in Section 7).

Fig. 5F shows an example of a box fold that has nearly vertical limbs and a flat top surface. They differ from folds shown in Fig. 5E in that they exhibit kink-fold geometry with sharp hinge zones. The folds shown in Fig. 5F could be the early stage of structural development shown in Fig. 5D, in which thrusts may have already emerged at the surface and cut the limbs of the folds. Note that the flat top surface of the box fold shown in Fig. 5F is also deformed by minor folds that are parallel to the overall trend of the bigger box fold.

Fig. 5G displays an example of a left-slip ductile shear zone that consists of *en echelon* tension cracks and curved troughs and ridges. The curved troughs and ridges are interpreted as oroclinal folds that formed first as obliquely oriented extensional fractures and were later warped about vertical axes as a result of progressive left-slip shear deformation. Closely and evenly spaced ridges parallel to the inferred shear-zone margins are interpreted as an expression of shear foliation created by left-slip shear. The high temperatures (180–200 K) along the TSF (e.g., Goguen et al., 2013) require that the homologous temperatures of the wall ice directly against the TSF fissure zones are up to 0.73. Under such temperature conditions, fine-grained ice aggregates would experience crystal-plastic deformation via dislocation creep (see summary by Kohlstedt and Mackwell, 2010 and references therein), which caused the development of planar ice fabrics defined by the preferred crystal growth and flattening of pre-existing pore spaces in the ice. Drag folds also appear to be present outside the shear zone, expressed by curved ridges and troughs that become parallel to the shear zone as they approach it. The inferred width of the shear zone is >20 km, which testifies to the important role of distributed deformation across the South Polar Terrain.

Fig. 5H provides an example of interactions between a pre-existing weakness and younger fractures. As shown in this image, one set of tension fractures (site 1) trends perpendicular to and terminates at the ASM. The same set of tension fractures also cuts across a group of parallel but curved ridges and grooves (site 3) that are interpreted as drag folds associated with right-slip motion along the ASM. We infer that the curved ridges and grooves were probably generated first by the formation of linear horst–graben systems under extension and were later modified by oroclinal folding. This is because the grooves are bounded by steep cliffs and flat trough floors, suggesting a graben origin. As no counterparts of the extensional zone can be found on the other side of the ASM, the tension fractures terminating at the ASM are interpreted to have developed after the initiation of the ASM. This relationship suggests that the ASM was mechanically weak during the formation of the tension cracks at site 1 (Cooke and Underwood, 2001). At site 2, tension cracks trending perpendicular to the ASM cut across the marginal zone. This relationship suggests that (1) their development postdates the fracture set at site 1, and (2) the frictional strength of the SSM was high (Cooke and Underwood, 2001) during the development of younger tension fractures. Note that ridges directly outside of the SPT display S-shaped traces (site 4 in Fig. 5H).

The SPT appears to locally preserve partially resurfaced pre-SPT structural fabrics. This is shown in Fig. 5I in which extensional cracks with similar trends, morphology, and lengths are present both within and outside the SPT. This observation suggests that the structures within the SPT result from deformation before and during the formation of this complex tectonic domain.

4. SPT marginal zone

The SPT boundary zone consists of the leading-edge, trailing-edge, sub-saturnian-edge, and anti-saturnian-edge margins (i.e., LEM, TEM, SSM, and ASM in Fig. 2). Their extents are delimited by the segmental ends shown as points A, B, C and D in Fig. 1. The marginal zone is locally cut by two types of fractures. Type-I fractures are Y-shaped with linear traces and terminate at the apexes of the arcuate segments of the SPT marginal zones (Porco et al., 2006) (Y-1 to Y-3 at the TEM in Fig. 1A). Type-II fractures are C-shaped fractures that lie orthogonal to the SPT margin, but display curved traces (i.e., C-1a, C-1b, C-2, and C-3 in Fig. 1A).

The SPT margin displays a total of 6 arcs (Fig. 1A), with the highest-curvature arcs associated with Y-shaped fracture zones along the TEM. Fractures in the individual Y-shaped zones were initiated at different times indicated by the cross-cutting relationships. For example, the Y-1a zone terminates at the outer arc whereas the Y-1b zone cuts into the inner arc of arc 3 (Fig. 6A–C). Similar relationships can also be established between arc 5 and extensional fractures in the Y-3 zone (Fig. 6E). However, given the available image resolution, we can only establish that major extensional fractures in the Y-2 zone terminate at the outer edge of arc 4 in Fig. 1A, but it is not clear if closely spaced extensional fractures cut into the marginal zone (Fig. 6D). In contrast to arcs along the TEM, arcs 1 and 2 along the LEM are not associated with any margin-perpendicular Y-shaped fractures (Fig. 6E and F). Instead, the LEM margin is characterized by a regional curvilinear escarpment and a local spoon-shaped scarp (Fig. 6F and G).

4.1. Leading-edge margin (LEM)

The LEM consists of sub-parallel and sharply crested ridges (Fig. 2A). Its outer edge is marked by an inward-facing scarp that displays two outward protruding arcs (arcs 1 and 2 in Fig. 2A). The outer edge also forms a sharp contact against heavily cratered terrains (site 10 in Fig. 2A) or curvilinear ridges and grooves (site 11 in Fig. 2A). The inner edge of the LEM separates well-organized parallel ridges within the marginal zone from complex ridge-groove regions inside the SPT (Fig. 2A). The inner edge is straight and not parallel to the outer edge of the marginal zone. The sharply crested ridges in the LEM zone display planar flanking slopes (Fig. 7), resembling normal fault scarps shown in Fig. 5C.

4.2. Trailing-edge margin (TEM)

The TEM zone is sub-parallel to and lies on the opposite side of the LEM (Fig. 2). The inner and outer edges of the marginal zone display sub-parallel curvilinear traces marked by four arc segments (i.e., arcs 3, 4, 5, and 6 in Fig. 1A). The ridges within the TEM zone display rounded tops and symmetric flanking slopes. Following the early work of Porco et al. (2006) and Spencer et al. (2009) and based on the criteria listed in Table 1, we interpret the ridges to have been generated by folding. The high-relief morphology of the fold-generated ridges in the trailing-edge zone contrasts sharply with the subdued topography and more complex patterns of fractures within the SPT (Fig. 2A).

4.3. Sub-saturnian-edge margin (SSM)

The SSM is bounded by a curvilinear outer edge and a transitional inner boundary (Fig. 2A). The marginal zone truncates a semi-circular depression (C1 in Fig. 2A) and several sub-parallel and curvilinear grooves (G1 in Fig. 2A) in the cratered terrains outside the SPT. The half circle (C1) feature is probably a relic of an impact crater that is cut by the SSM. However, no matching counterpart can be found within the SSM zone, suggesting the original topography has been obliterated due to SSM deformation. The older terrains display two prominent evenly spaced and parallel sets of extensional fractures: features F1 and F2 in Fig. 2A.

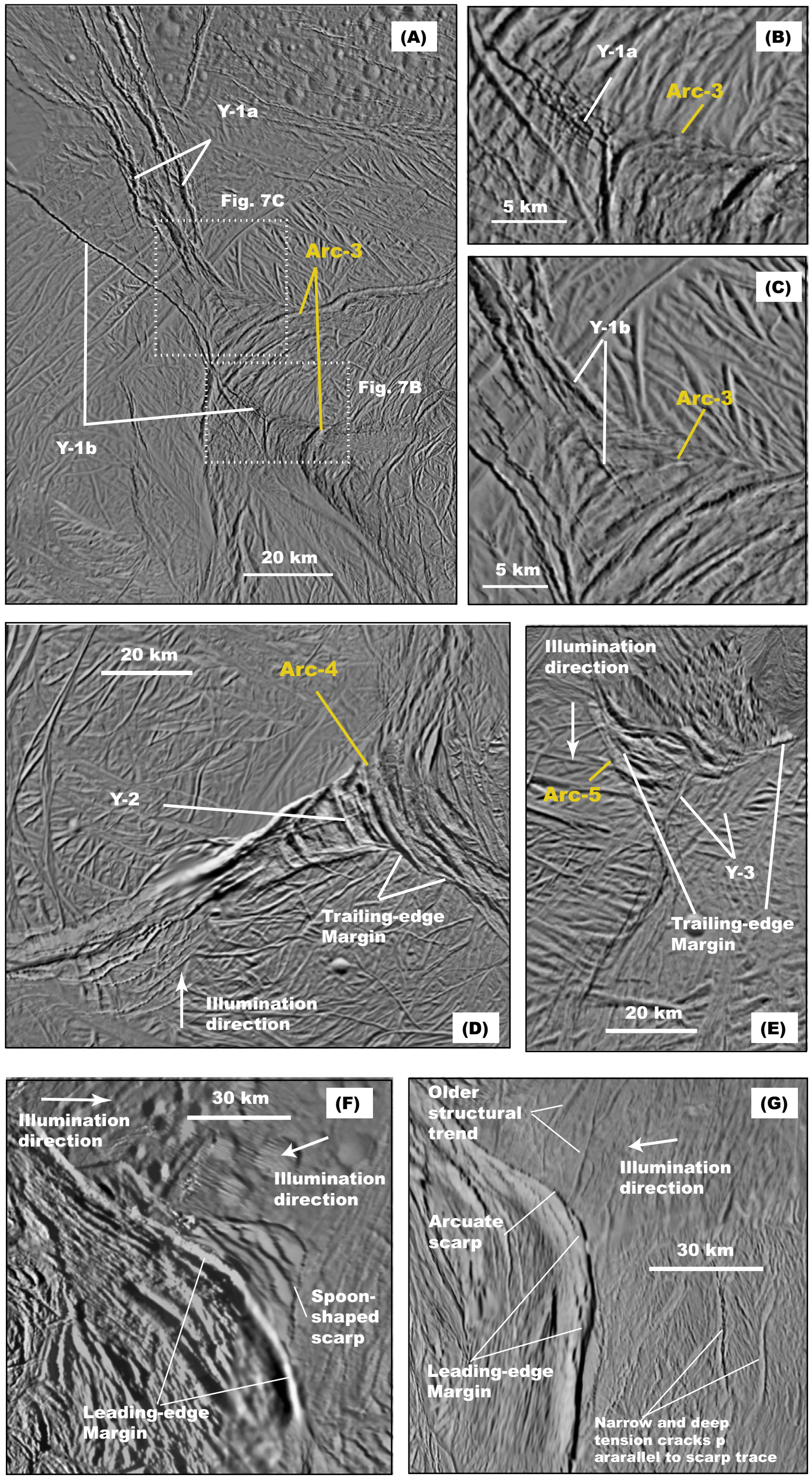

Fig. 6. The resolution of all the figures is 110 m/pixel. The top, bottom, left, and right sides of all the figures point toward the anti-saturnian, sub-saturnian, leading-edge, and trailing-edge directions. (A) Y-shaped fracture zone abuts an arcuate segment of the fold belt in the trailing edge margin (TEM). See Fig. 1A for location. (B) A close-up view of the relationship between a branch of a Y-shaped fracture zone and the outer part of an arcuate segment of the TEM fold belt. Note that the fractures in the Y-shaped zone terminate at the hook-shaped ridge-trough zone marking arc-3 in Fig. 1A. See (A) for location. (C) A close-up view of the relationship between a branch of a Y-shaped fracture zone and the inner part of an arcuate segment of the TEM fold belt. Note that some fractures in the Y-shaped fracture zone cut across the hook-shaped ridge-trough zone. Note that cracks in the Y-shaped fracture zone terminate the arc-shaped ridge-trough zone. See (A) for location. (D) Relationship between a Y-shaped extensional fracture zone and an arcuate segment of the TEM fold belt. Note some cracks in the Y-shaped fracture zone cut across the arc-shaped ridge-trough zone. See Fig. 1A for location. (E) Relationship between a Y-shaped extensional zone and an arcuate segment of the TEM fold belt. See Fig. 1A for location. (F) An arcuate segment of the leading-edge margin that separates the highly faulted zone within the SPT from heavily cratered region outside the SPT. Note that the spoon-shaped normal fault zone is truncated by the younger and through-going escarpment marking the main trace of the LEM. See Fig. 1A for location. (G) An arcuate segment of the leading-edge marginal (LEM) of the SPT that separates a highly faulted region inside the SPT and a region consisting of closely spaced ridges and troughs that are oriented at high angles and truncated by the LEM escarpment. See Fig. 1A for location.

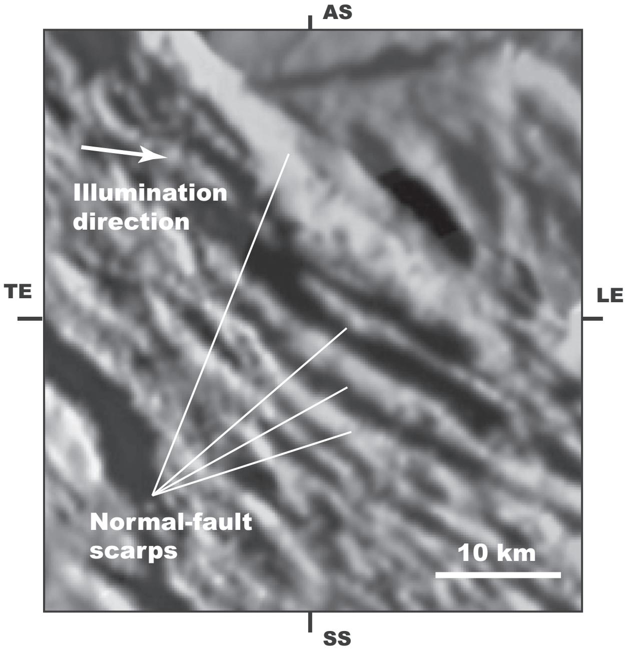

Fig. 7. Image of interpreted normal faults defined by planar scarps in the leading-edge margin (LEM). See Fig. 1A for location.

The SSM displays a right-step bend at location 1 and a left-slip bend at location 2 in Fig. 2A. Although curvilinear bends are common along all four sides of the SPT, the structures across the two bends in the SSM zone are oriented obliquely, rather than parallel to the edge of the margin; this is similar to the oblique secondary structures in the ASM zone, but different from secondary parallel structures in the TEM and LEM zones (Fig. 2A and B). Along the right-step bend, the outer contact of the marginal zone is sharp (feature 1 in Fig. 8A) and separates the high-relief ridges in the marginal zone (features 2 and 3 in Fig. 8A) from low-relief regions in the older terrains outside the SPT. In contrast, the inner contact of the SSM is transitional, which is expressed by *en echelon* ridges in the marginal zone that extend into the SPT interior (Fig. 2A). As the high-relief ridges display rounded ridge tops and symmetric flanking slopes, we interpret them to have been originated from folding. The ridge traces display "lazy-Z" shapes in map view identified as features 2 and 3 in Fig. 8A, indicative of oroclinal folding in a left-slip shear zone. The oblique orientation of the interpreted fold-generated ridges is consistent with left-slip deformation in the SSM zone. The curved ridges shown as features 2 and 3 in Fig. 8A are cut by closely spaced parallel extensional fractures that are oriented at high angles to the SSM (i.e., features 4a and 4b in Fig. 8A). Some of the extensional fractures appear to terminate at the ridges, based on the currently available image resolution.

Fig. 8B displays linear ridges (feature 2) in the right-step bend oriented obliquely to the SSM (feature 1). The linear ridges display planar flanks interpreted as normal-fault scarps. This interpretation implies that the SSM zone has experienced left-slip shear deformation. The left-slip-shear interpretation is consistent with the geometry of curved ridges and troughs against the SSM zone, shown as feature 3 in Fig. 8B. The curved ridges have rounded tops and thus are interpreted to have originated by folding. Together with observations shown in Fig. 8A, we interpret the left-step and right-step bends in the SSM zone as a restraining and releasing bend, respectively, in a broad left-slip shear zone.

4.4. Anti-saturnian-edge margin (ASM)

The ASM is bounded by a sharp scarp on its outer edge (feature 1 in Fig. 9A and feature 1a in Fig. 9B) and a semi-continuous ridge as an inner edge (feature 2 in Fig. 9A and feature 1b in Fig. 9B). The width of the marginal zone changes drastically along its trend: from less than a few hundreds of meters along the trailing- and leading-edge segments to ~12 km along the central segment (Fig. 9A). The morphology of the ASM zone is characterized by the presence of continuous, sub-parallel, and closely spaced ridges (feature 5 in Fig. 9B). A right-slip shear zone sub-parallel to the ASM exists along the interior part of the ASM zone. The sense of shear is indicated by the presence of drag folds (features 7 and 8 in Fig. 9B) and *en echelon* extensional fractures trending obliquely to the general trend of the ASM zone (i.e., feature 3 in Fig. 9A).

Some troughs inside the SPT are curved as they approach the ASM zone (features 2 and 4 in Fig. 9B), whereas others remain straight (feature 6 in Fig. 9B). Similarly, curved (feature 3a) and straight (feature 3b) troughs are also present outside the SPT against the ASM zone (Fig. 9B). The curved geometry of feature 3 outside the SPT and features 2 and 4 inside the SPT indicate right-slip shear along the ASM and its neighboring deformation zone. This interpretation requires that the curved troughs and ridges represented by features 2 and 4 were originally straight. We suggest that the curved ridges and troughs were developed when the ice shell near the ASM was still soft, whereas the straight ridges and troughs formed when the ice shell became hardened possibly due to cooling, which led the ridges and troughs to be resistant to the drag effects induced by right-slip motion along the ASM.

Within the ASM zone, a group of closely spaced (<1–2 km) and sub-parallel ridges are oriented obliquely in the marginal zone (feature 5 in Fig. 9B). These ridges display "rope-like" morphology, similar to those described by Barr and Preuss (2010), and are interpreted here as folds. Their oblique orientation (i.e., feature 5 in Fig. 9B) requires right-slip shear along the ASM. Feature 6 in Fig. 9B is a sharp planar scarp interpreted as a normal fault (also see Fig. 5C). Its oblique orientation requires right-slip shear along the ASM zone. Right-slip shear along the ASM zone is also indicated by a kinematically linked right-slip shear zone (feature 8 in Fig. 9B), which hosts a set of *en echelon* extensional fractures (feature 7 in Fig. 9B). The presence of drag folds, expressed by abrupt turns in the trend of troughs (feature 9 in Fig. 9B), is consistent with the interpreted right-slip movement of the shear zone linked with the ASM.

The ASM zone truncates several sets of extensional fractures (features 4, 6, and 7 in Fig. 9A); the most prominent are features 1 and 2 in Fig. 9C cutting across and terminating at the ASM zone, respectively. Note that segments of the extensional fractures (feature 2 in Fig. 9C) outside the SPT are bent and the curved geometry is consistent with a right-slip sense of shear. Although both sets of fractures die out ~10 km away from the ASM zone inside the SPT interior (Fig. 9A), the fractures that cut across the ASM zone extend >60 km outside the SPT (C-3 in Fig. 1A and feature 5 in Fig. 9A).

There are at least three possible explanations for the observed cross-cutting relationships between the ASM zone and the zones of closely spaced extensional fractures (Fig. 10). First, the ASM could be a pre-existing feature, and ASM-parallel extension created orthogonally oriented fractures that terminate at the weaker segment of the ASM fault (i.e., feature 1 in Fig. 9C) but cut across the strong segment of the marginal zone (i.e., feature 2 in Fig. 9C), as predicted by the model proposed by Cooke and Underwood (2001) (Fig. 10A). This interpretation implies that the development of the ASM zone is unrelated to the formation of the extensional fractures. The mechanism as shown in Fig. 10A, however, predicts closely spaced extensional fractures that

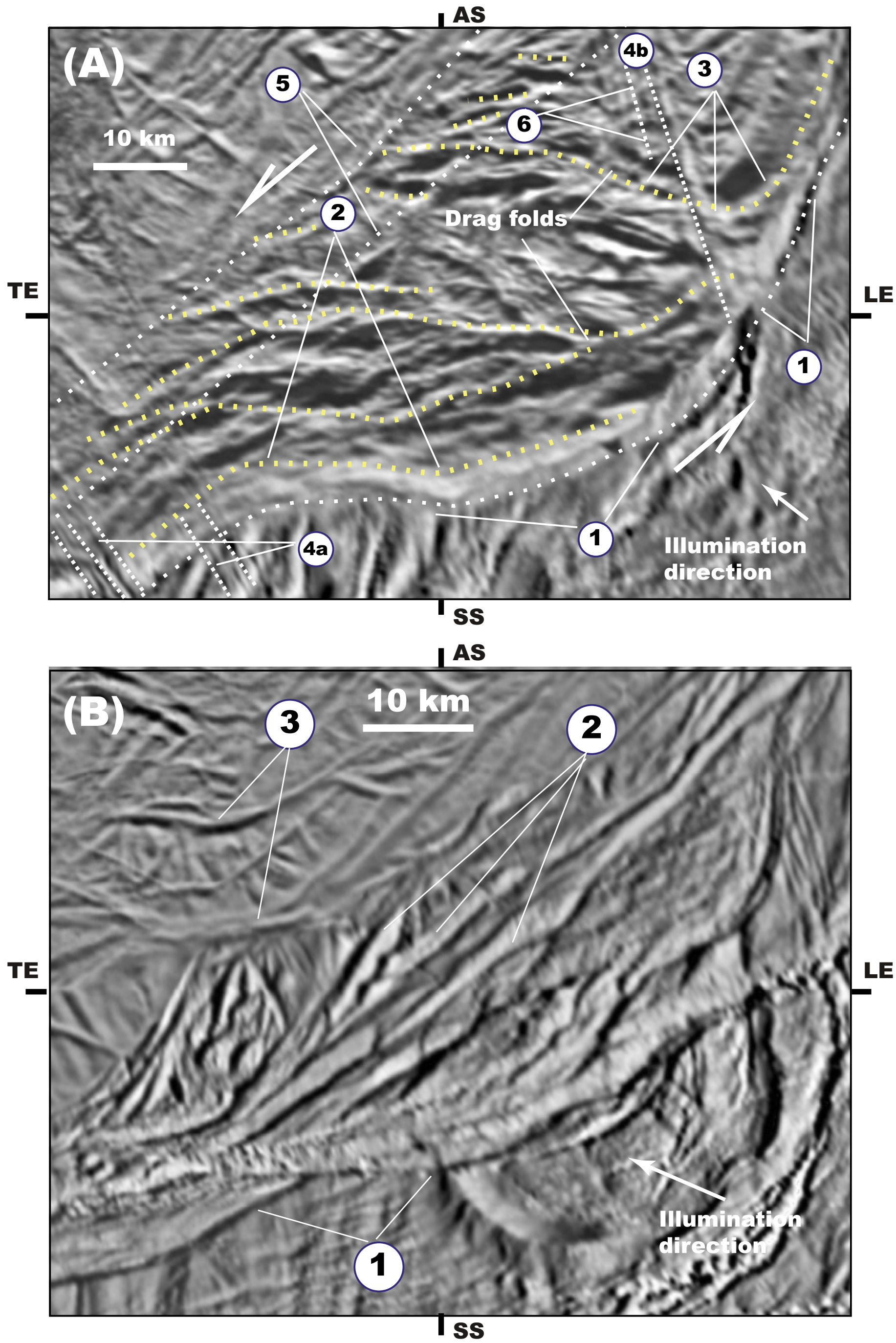

Fig. 8. (A) Image of a transpressional system within the left-slip sub-saturnian margin of the SPT. See Fig. 1B for location, numbers are features discussed in the text. (B) Image of a transtensional system in the sub-saturnian margin of the SPT. Numbers refer to features discussed in detail the text. See Fig. 1B for location.

terminate at the ASM zone (i.e., feature 1 in Fig. 1C) should be present both inside and outside the SPT against the ASM. However, this prediction is inconsistent with the observation that the terminating fractures are only present within the SPT. Because of this discrepancy from the predicted cross-cutting relationship, we consider the scenario in Fig. 10A unlikely.

Second, the fracture set terminated at the ASM zone (i.e., feature 1 in Fig. 9C) may have been generated early during ASM-parallel extension within the SPT only; this extension induced right-slip motion on the ASM zone (stages 1 and 2 in Fig. 10B). Subsequently, the ASM zone and its neighboring regions experienced ASM-parallel extension, creating orthogonally oriented fractures (i.e., feature 2 in Fig. 9C) cutting across the marginal zone (stage 3 in Fig. 10B). One prediction of this kinematic model is that the younger, through-going fracture set should cut the older fractures terminated at the ASM zone, which is not consistent with the observation shown in Fig. 9C.

Third, the development of extensional fractures propagating from outside the SPT toward the interior of the SPT was perhaps intermittently interrupted by right-slip shear along the ASM zone (Fig. 10C). The scenario shown in Fig. 10C predicts that the fractures outside of the SPT should have accommodated more extension, as shown by the increasing line width in the figure. This prediction is consistent with the observation that the extensional

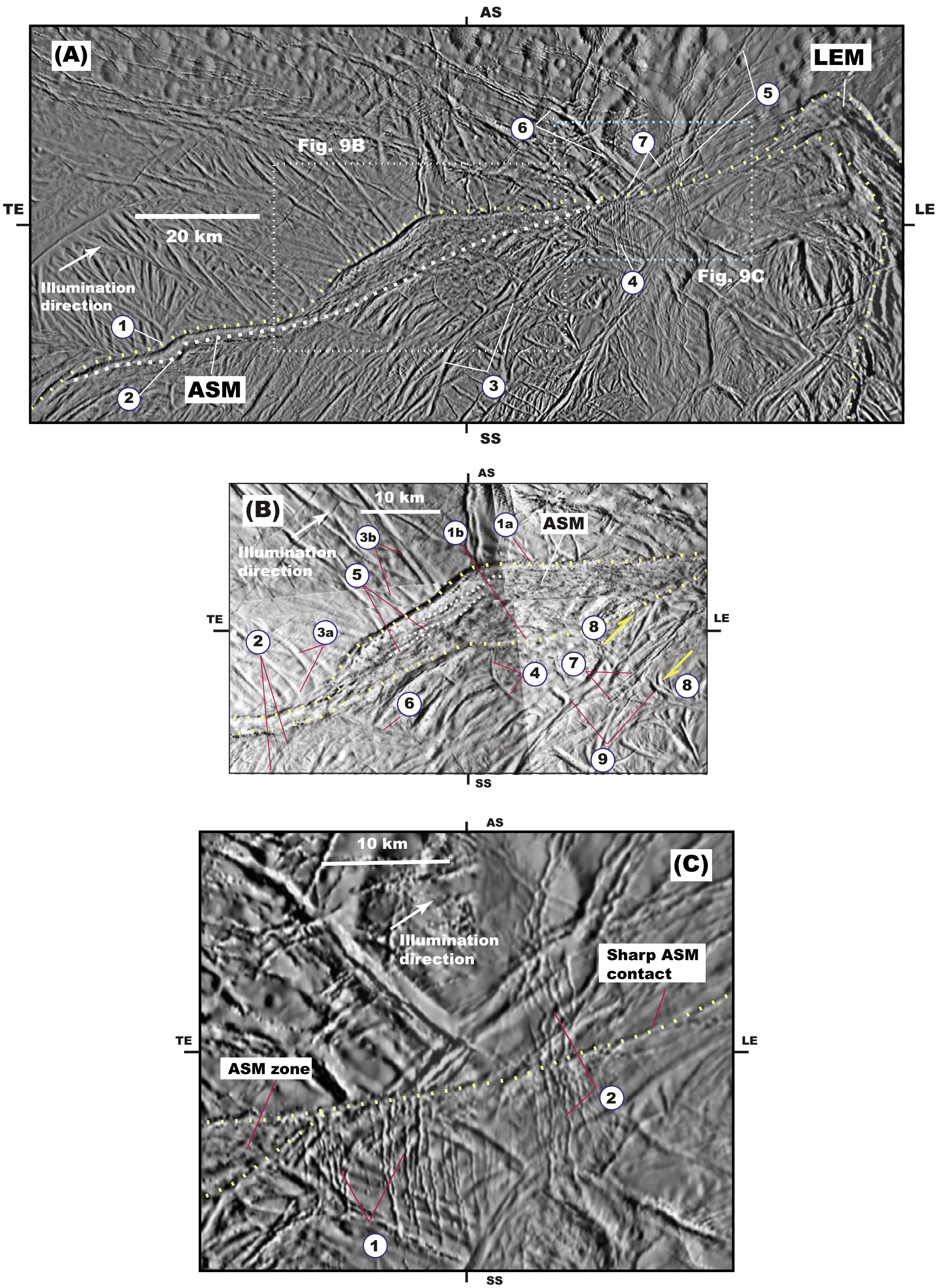

Fig. 9. (A) Image of the anti-saturnian margin (ASM) and its relationship to the leading-edge margin (LEM). Numbers refer to features discussed in the text. See Fig. 1B for location. (B) Image of the central segment of the ASM. Numbers refer to features discussed in the text. See (A) for location. (C) Relationships among orthogonally oriented extensional fracture zones and the sharply defined segment of the ASM. Numbers refer to features discussed in the text. See (A) for location.

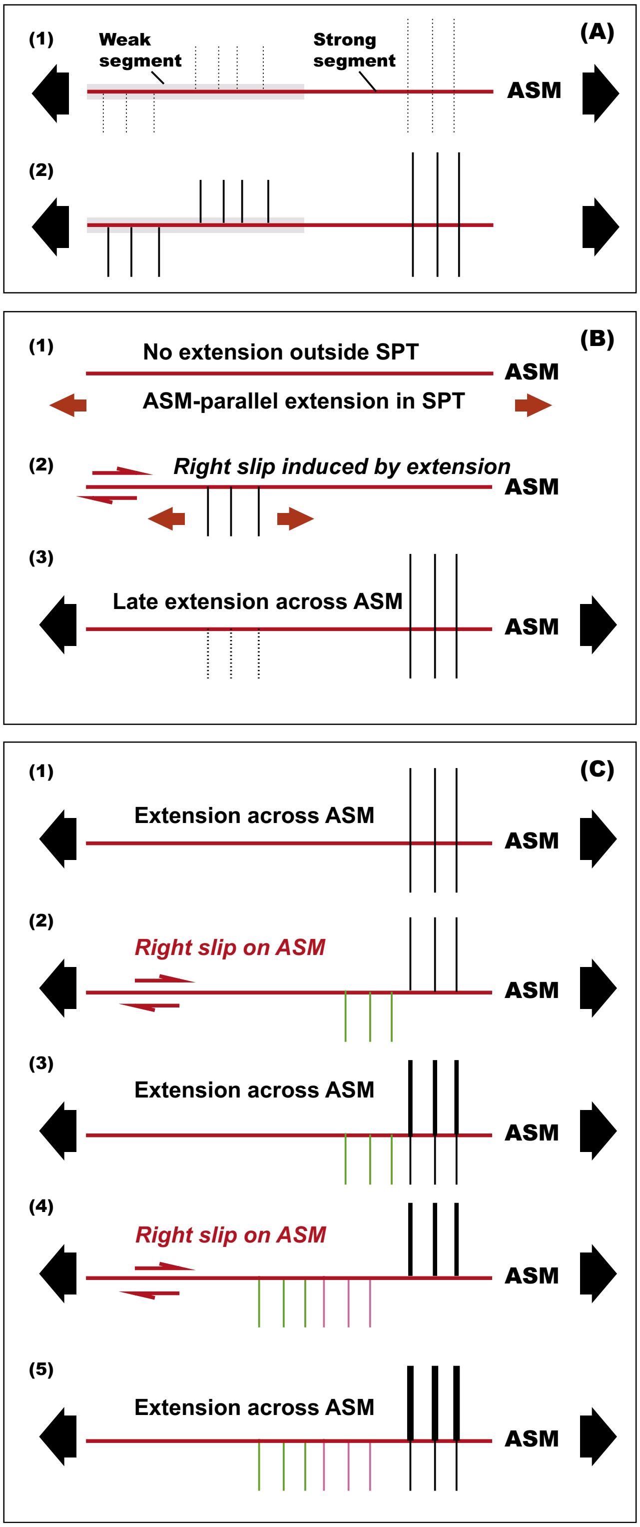

Fig. 10. Three possible scenarios for alternating development of extensional fractures terminating at and cutting across the anti-saturnian margin (ASM). See text for details. Note that the two thick red arrows below the horizontal fracture in B2 show the direction of wall-rock extension, which produced the extensional cracks. Extension in turn induces right-slip shear along the left segment of the horizontal fracture. (For interpretation of the references to color in this figure legend, the reader is referred to the web version of this article.)

fractures outside the SPT (feature 2 in Fig. 9C) are expressed by wider and deeper troughs than those inside the SPT. This alternating process produced a wide fracture zone within the SPT and a narrow fracture zone outside the SPT. Because the process shown in Fig. 10C best explains the observed cross-cutting relationships and morphology of the fractures (feature 2 in Fig. 9C) cutting across the AMS, we believe that this is probably the most likely scenario. An important implication of the scenario shown in Fig. 10C is that the fault alternates in its strength from being strong allowing fractures to cut across to being weak allowing the cross-cutting fractures to be offset by the ASM fault. This alternation in frictional strength with time may be explained by the experimental results of Schulson and Fortt (2013). These authors show that the coefficient of friction of a shear surface increases with the increase in the duration of inactivity of the shear surface. Thus, the fault is weak when the fault moves more frequently, while it is strong when it slips less frequently.

An obvious question is why the margin-orthogonal extensional fractures form at all. As discussed below, the extensional fractures could have originated in two ways. (1) They were generated by a regional stress field outside the SPT and this stress interacted with the local stress field of the SPT across the ASM boundary. (2) They formed as a result of the overall SPT development, and the margin-orthogonal extensional fractures were induced by the overall extension in the trailing-edge and leading-edge direction parallel to the ASM (see detailed description of our gravitational spreading model in Section 7).

5. Tiger-stripe fracture zones

The TSF are the most dominant structures within the SPT. The fractures terminate before reaching the SPT margin and the structures between the TSF termination and the marginal zone are complex, characterized by multiple phases of fracture development (e.g., Patthoff and Kattenhorn, 2011) and different styles of deformation than those in the TSF-bounded region (Figs. 1 and 2). The complexity in the transition zone from the TSF to the SPT margin may have resulted from the preservation of pre-SPT-development structures.

5.1. Alexandria fracture zone

The curvilinear Alexandria fracture terminates at hook-shaped (Porco et al., 2006) ridge-trough zones at its two ends (Figs. 2A, 11A and B). The hook-shaped ridges that are 200–400 m wide have rounded ridge tops and symmetric ridge flanks (features *3* and *4* in Fig. 11A); they are thus interpreted as folds following the criteria outlined in Table 1. The ridges parallel to and at the end of the Alexandria fracture are merging and diverging at small angles (~a few degrees) along strike (feature *1* in Fig. 11A). At the first glance, these ridges appear to have similar morphology as the double ridges bounding the Alexandria and other tiger-stripe fracture zones. However, detailed examination reveals several key differences. The ridges bounding Alexandria are (1) much wider (>2 km in width), (2) laterally continuous along the entire fracture zone, and (3) asymmetric in cross section with short and steep slopes bounding the tiger-stripe fractures and long and gentle slopes away from the tiger-stripe fractures. More importantly, the surfaces of the double ridges bounding the tiger fracture are much smoother than those of the hook-shaped ridges at the ends of the Alexandria fracture; the smooth surface texture of the double ridges may be induced by transient sublimation events along the fissure zone (Goguen et al., 2013) and/or deposition of ice grains from vapor jets (e.g., Spencer et al., 2009).

A fracture zone branching off from the Alexandria fracture (feature *e* Fig. 2A) terminates at a perpendicular zone of ridges that display fold morphology (feature *f* in Fig. 2A). Parallel fractures branching off from the Alexandria zone (feature 4 in Fig. 11B) cut

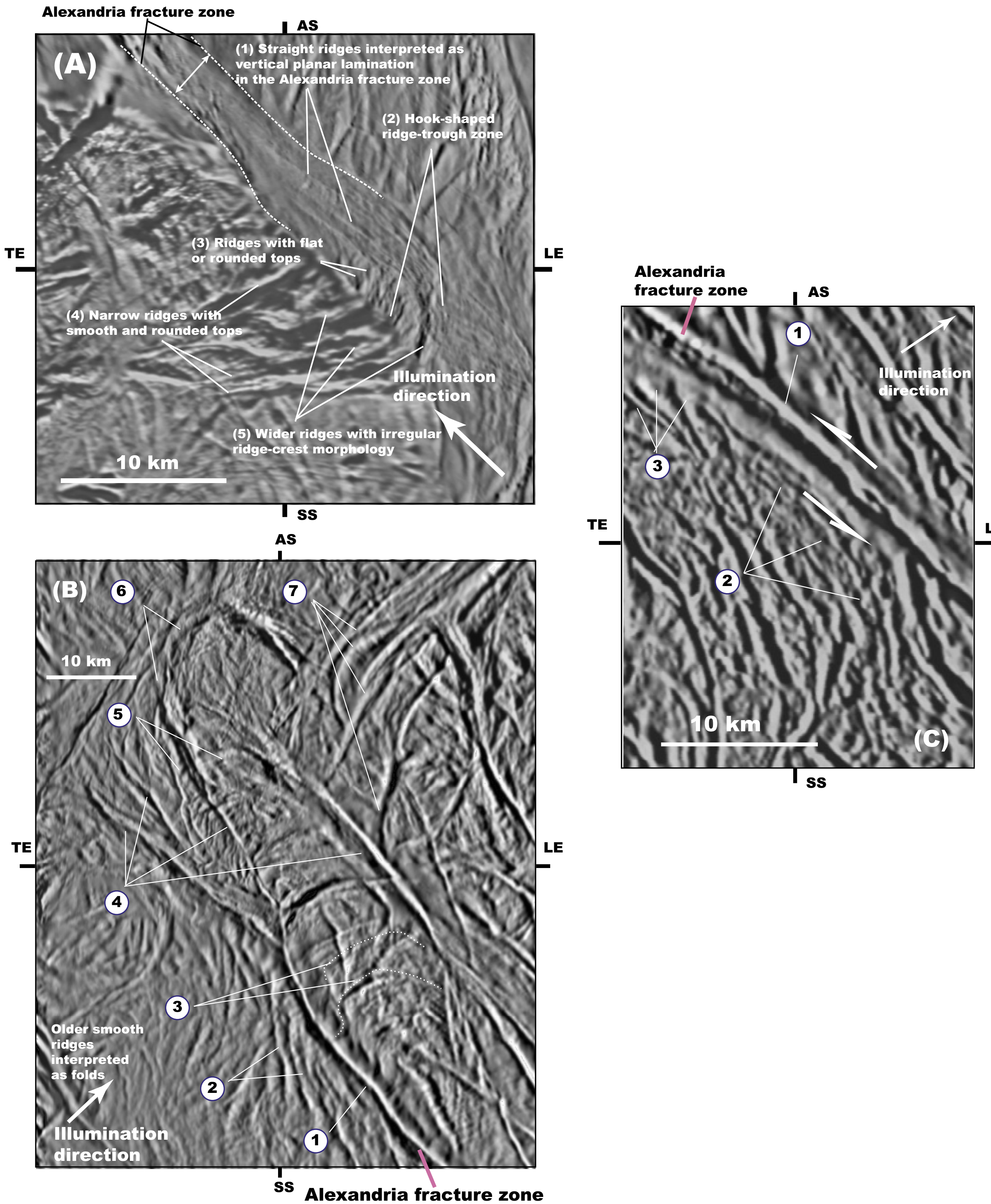

Fig. 11. (A) Structures at the sub-saturnian and (B) anti-saturnian terminations of the Alexandria fracture zone. See Fig. 1B for location. (C) Closely spaced and rounded-top ridges interpreted as folds. Their curvilinear traces are interpreted as oroclinal folds generated by left-slip shear along the Alexandria fracture zone. Numbers refer to features discussed in the text. See Fig. 1B for location.

across orthogonally oriented curved ridges, which are interpreted as folds (features 5, 6, and 7 in Fig. 11B). Based on the similar hook-like geometry, we interpret the perpendicular ridges cut by young fractures to have been related to early development of TSF-like fractures that were abandoned as the termination zone migrated toward the interior of the SPT. This interpretation in turn implies repeated development of TSF-parallel fractures and their termination at a series of hook-shaped fold zones of different ages.

The sub-saturnian segment of the Alexandria fracture zone consists of a zone of closely spaced, straight ridges and troughs (feature *1* in Fig. 11A). Their straight traces, close spacing, and parallelism to the Alexandria fracture lead us to interpret them to represent shear planes and/or shear surfaces. Termination at the hook-shaped fold belt (features *2*, *3*, and *4* in Fig. 11A) requires left-slip shear along the Alexandria fracture zone.

Obliquely oriented fold ridges characterized by rounded ridge tops intersecting the anti-saturnian segment of the Alexandria shear zone die out away from the shear zone (feature *2* in Fig. 11B). The rounded-top ridges are interpreted as folds and their orientation requires left-slip motion along the Alexandria shear zone. Closely spaced, low-relief, and hook-shaped ridges in a broad depression are linked with the Alexandria shear zone (feature *3* in Fig. 11B). Smooth-topped ridges in the hook-shaped zone are interpreted as folds, which again require the Alexandria shear zone to be a left-slip structure.

Along the central segment the Alexandria fracture zone (feature *1* in Fig. 11C), several ridges and troughs branch off from the fracture zone and display oroclinal fold geometry in map view (feature *2* in Fig. 11C). These oblique ridges with rounded tops are interpreted as folds; their orientation is indicative of left-slip motion along the Alexandria shear zone (e.g., Sylvester, 1988). In addition, three round-top ridges branching off from and orientated obliquely to Alexandria (feature *3* in Fig. 11C) suggests left-slip motion on the Alexandria shear zone. The segments of feature *2* ridges parallel to the Alexandria fracture in Fig. 11C are interpreted as a result of left-slip shear, which have rotated the originally oblique folds into parallelism to the shear zone.

5.2. Cairo fracture zone

The curvilinear Cairo fracture (feature *g* in Fig. 2A and feature *1* in Fig. 12A) is bounded by flanking ridges with steep scarps facing

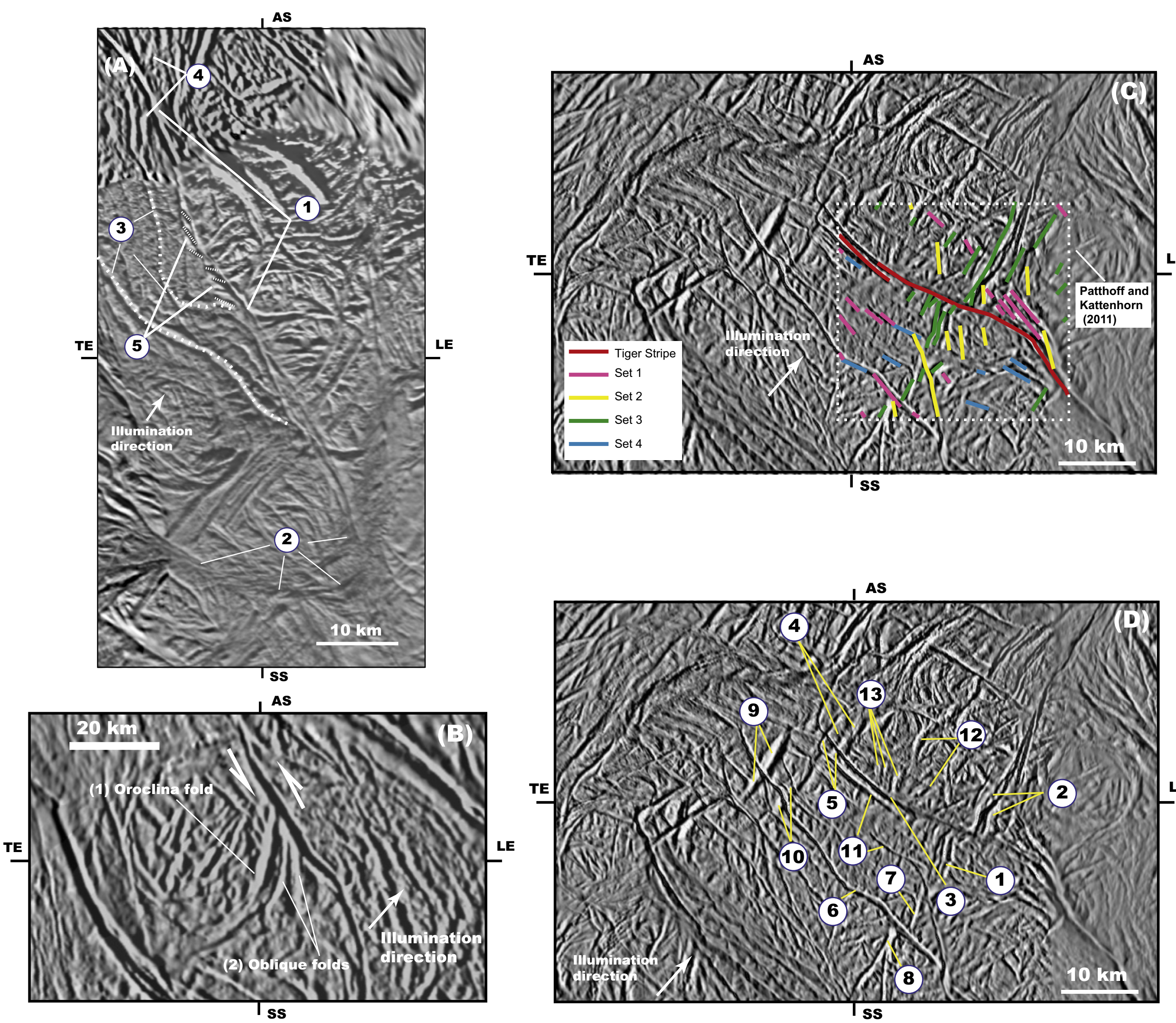

Fig. 12. (A) Sub-saturnian segment of the Cairo fracture zone and its linking hook-shaped structures. See Fig. 1A for location. (B) Horsetail-like structures along the sub-saturnian segment of the Cairo fracture zone. See Fig. 1A for location and text for detailed description. (C) Anti-saturnian segment of the Cairo fracture zone and adjacent minor structures. Colored lines are adopted from Patthoff and Kattenhorn (2011) and represent four interpreted phases of deformation. (D) Uninterpreted image across the anti-saturnian segment of the Cairo fracture zone. Numbers refer to features discussed in detail in the text. See Fig. 1A for location and text for detailed description and interpretations. (E) Four different scenarios for the development of fracture patterns shown in (D). See text for details. (For interpretation of the references to color in this figure legend, the reader is referred to the web version of this article.)

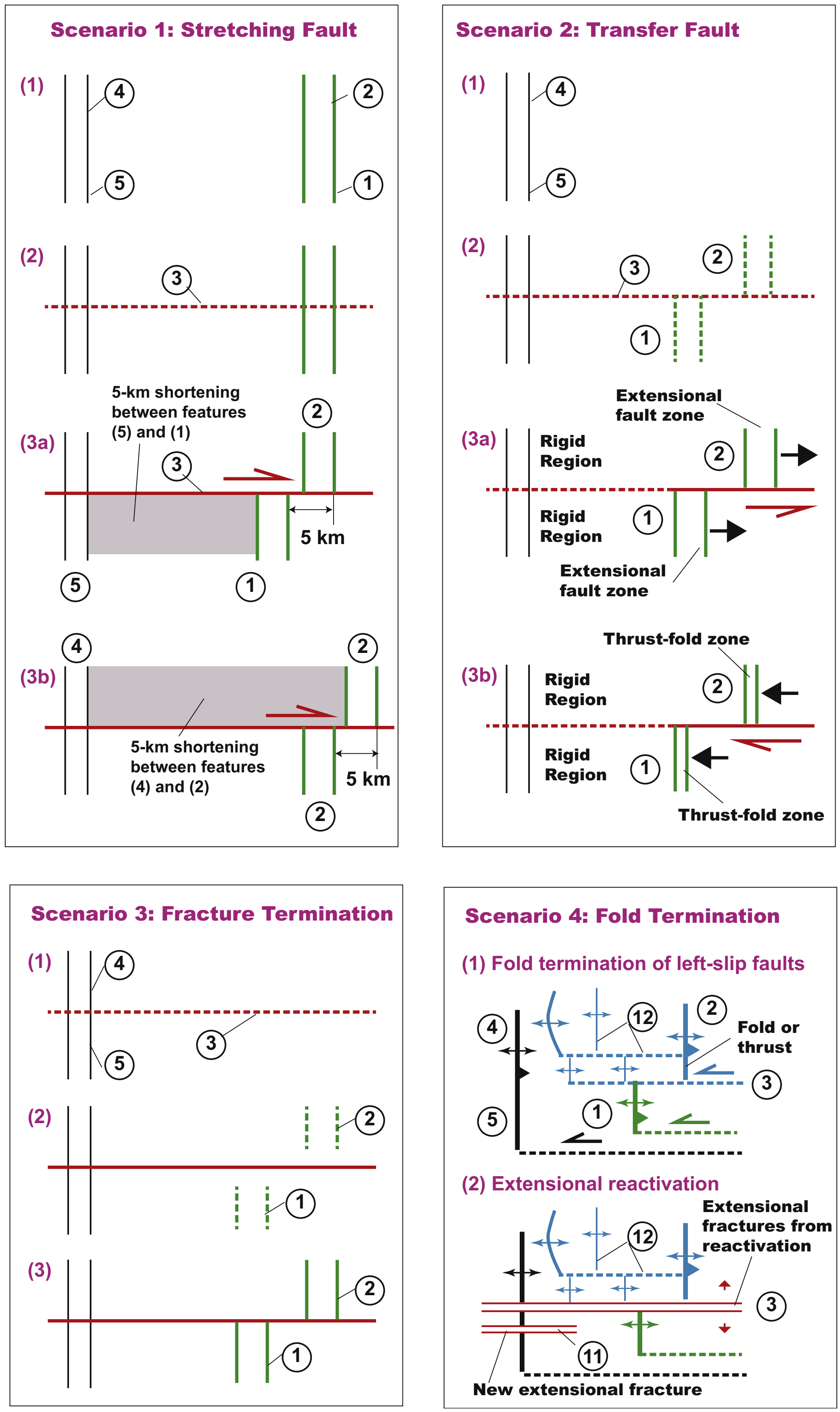

Fig. 12 (*continued*)

the fracture zone and gentle slopes away from the fracture zone. The Cairo fracture zone also truncates nearby curvilinear ridges and troughs that display asymmetric oroclinal-fold geometry (feature *13* in Fig. 2A); the asymmetry of the oroclinal fold is indicative of left-slip shear in map view. The sub-parallel geometry of the oroclinal folds and the Cairo fracture zone may indicate the two features were oroclinally warped together about the same vertical axis (i.e., bending of pre-existing linear fracture zones into curved fracture zones in map view). Alternatively, the curvature of the Cairo fracture zone may have controlled the formation of oroclinally folded ridges, much like the formation of fault-bend folds in cross-section view (Suppe, 1983).

We interpret here the Cairo fracture zone to be a left-slip structure. Evidence supporting this interpretation includes: (1) termination of the fracture zone at orthogonally oriented straight and hook-shaped ridges that have rounded tops and symmetric flanking slopes and are interpreted as folds (feature *4* in Fig. 2A and feature *2* in Fig. 12A), (2) the presence of oroclinal drag folds next to the fracture zone (feature 3 in Fig. 12A), (3) obliquely oriented folds (feature *4* in Fig. 12A), and *en echelon* extensional fracture zones (feature *5* in Fig. 12A), and (4) a major secondary fracture branching off from the Cairo fracture zone and displaying a horsetail geometry (feature *12* in Fig. 2A and features *1* and *2* shown in Fig. 12B). The positive topography and rounded ridge tops suggest that the termination horsetail structures (i.e., ridges) are folds; their orientation requires left-slip shear along this structure secondary to the main Cairo fracture zone. The secondary left-slip fracture zone is interpreted as a P-shear (Sylvester, 1988) developed coevally with the left-slip Cairo fracture zone.

Locally available high-resolution images indicate that structures at the anti-saturnian segment of the Cairo fracture zone are complex, characterized by complex termination and cross-cutting relationships (Fig. 12C and D). Patthoff and Kattenhorn (2011) propose four phases of deformation in the region, with global significance across Enceladus; each phase is marked by the development a unique set of linear fractures (Fig. 12C). These authors further suggest that the formation of the youngest fracture set was coeval with the TSF initiation. In this study, we reexamine the proposed cross-cutting relationships by Patthoff and Kattenhorn (2011) and find that their assigned sequence and kinematics of fracture formation are non-unique. Below we use their proposed right-slip offset along the Cairo fracture zone as an example to illustrate the issue.

Patthoff and Kattenhorn (2011) suggest that features *1* and *2* are offset by a fault shown as feature *3* in Fig. 12D (see Fig. 2 in Patthoff and Kattenhorn, 2011). Placing their interpretation in a larger contest, we find that feature *3*, if interpreted as a right-slip fault zone as suggested by the authors, does not offset linear ridges and troughs toward the anti-saturnian direction (features *4* and *5* in Fig. 12D). A similar observation can be made along a fracture zone represented by feature *6* in Fig. 12D, which displays apparent right-lateral offsets of features *7* and *8* but not features *9* and *10* in Fig. 12D. This contradiction may be explained by four different scenarios as discussed below (Fig. 12E).

(1) In the stretching-fault (e.g., Means, 1989) explanation (scenario 1 in Fig. 12E), feature *3* in Fig. 12D is a fault whose motion accommodates coevally deforming fault-bounded wall rocks. Such a fault is characterized by a systematic decrease in offsets toward the fault tips at which fault slip should be zero. In this case, features *1* and *2* should have formed as a single linear feature prior to the formation of feature 3; the combined linear ridge composed of features *1* and *2* was later offset for $\sim$5 km right laterally, as proposed by Patthoff and Kattenhorn (2011). As features *4* and *5* are not offset along the same "feature *3*" fault, the right-slip motion must be accommodated by fault-parallel extension on the anti-saturnian side of the fault (stage 3a in scenario 3 of Fig. 12E), or fault-parallel shortening on the sub-saturnian side of the fault (stage 3b in scenario 3 of Fig. 12E). A detailed examination of Fig. 12D suggests the absence of those required structures. Specifically, the two rounded-top ridges (feature *2* in Fig. 12D) represent two individual anticlinal folds. The presence of the two anticlines requires that the deep trough separating the two anticlines must be a synclinal fold rather than an extensional fracture as proposed by Patthoff and Kattenhorn (2011). The lack of planar scarps, required by the extensional-fracture interpretation of Patthoff and Kattenhorn (2011), along the two sides of the anticlinal ridges further supports the synclinal-fold interpretation.

(2) In the transfer-fault explanation (scenario 1 in Fig. 12E), orthogonally oriented extensional zones, represented by features *1* and *2* in Fig. 12D, were created simultaneously during the formation of feature *3* as an accommodation fault in an extensional zone. This model requires that one segment of the fault be active, linking the two apparent offset features via left-slip or right-slip faulting (scenario 2 in Fig. 12E). The model does not explain why the "feature 3" fault, extending beyond the two apparent offset markers, cut across features *4* and *5* without offsetting them.

(3) In the fracture-termination explanation (scenario 3 in Fig. 12E), the apparent offset of features *1* and *2* in Fig. 12D formed after the formation of feature *3* in Fig. 12D. Features 1 and 2 formed as faults and their propagation was impinged by preexisting feature 3 (scenario 3 in Fig. 12E). In this scenario, features 1 and 2 are the youngest structures and contradict the inferred fracture-formation sequence by Patthoff and Kattenhorn (2011).

(4) The fold-termination explanation requires the Cairo fracture zone and parallel fractures to be left-slip faults and their linked perpendicular ridges and troughs to be folds (scenario 4 in Fig. 12E). This geometric model explains the presence of linear topographic highs associated with depressions that were interpreted as fractures by Patthoff and Kattenhorn (2011). For example, features *1* and *2* are both broad linear uplifts with linear fissures cutting across the ridge crests. In the fold-termination model, these fissures could be surficial fractures generated along fold crests. Alternatively, they could the high-amplitude synclinal folds, creating deep troughs. As features *4* and *5* are not laterally offset, the interpreted left-slip faults must have been reactivated by extension (scenario 4 in Fig. 12E). The proposed late extension would also explain the formation of parallel strike-slip faults such as feature *11* in Fig. 12D.

In summary, the complex geometric relationships at the anti-saturnian end of the Cairo fracture zone could be interpreted in multiple ways, each implying different mechanical origins and formation sequences of the fractures. When the predictions of the models are tested against the observations, we favor scenarios 3 and 4 as the most plausible mechanisms to explain the observed fracture pattern shown in Fig. 12D. In either case, an extensional event is required along the Cairo fracture zone that postdates its left-slip motion.

5.3. Baghdad fracture zone

The Baghdad fracture zone bounds oroclinally warped folds indicative of broad left-slip shear (feature *3* in Fig. 2A). The fracture zone bifurcates in the sub-saturnian direction into two branches (features *14a* and *14b* in Fig. 2A), each displaying narrow troughs (feature *1* in Fig. 13A and features *1* and *2* in Fig. 13B). The troughs are bounded by raised flanks or ridges. Obliquely oriented *en echelon* tensile cracks (feature 2 in Fig. 13A) lie within the fracture zone labeled as feature *14a* in Fig. 2A, which indicates left-slip shear. Feature *14a* as a fracture also splits into a sharp-crested linear ridge with a planar scarp (feature *3* in Fig. 13A points to the sharp scarps bounding the ridges) and a curved trough (feature *4* in Fig. 13A). The curved trough bounds a highland marked by curved and fold-generated ridges. The interpreted folds are subparallel to the curved bounding trough, suggesting that the base

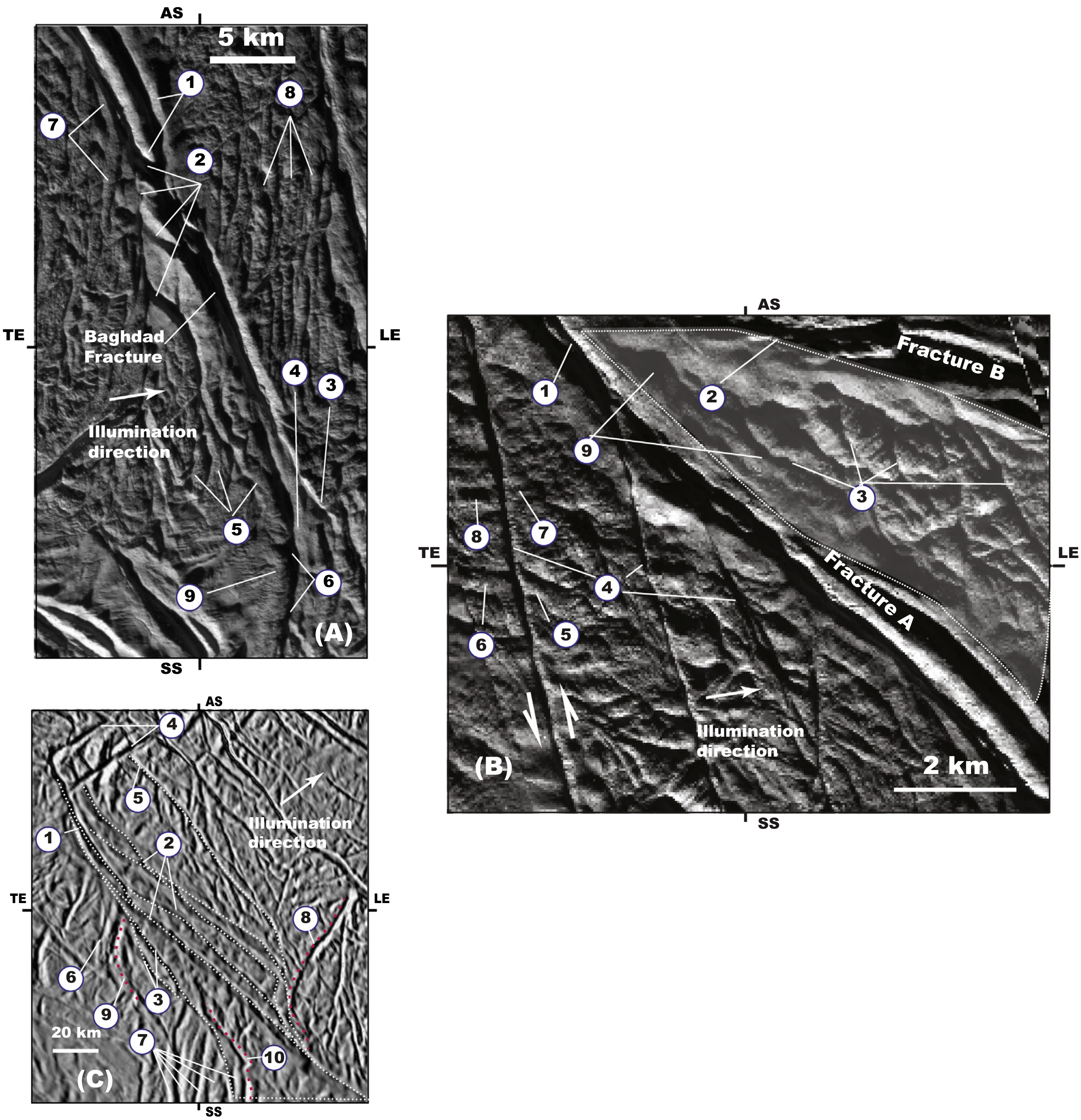

Fig. 13. (A) Oblique folds and *en echelon* extensional fractures against or within the Baghdad fracture zone. See Fig. 1A for location. (B) Minor structures against the two branches of the Baghdad fracture zone. Numbers refer to geologic features discussed in detail in the text. See Fig. 1A for location. (C) Minor structures against the anti-saturnian segment of the Baghdad fracture zone. Numbers refer to geologic features discussed in detail in the text. See Fig. 1A for location.

of a raised flank (feature *9* in Fig. 13A) is bounded by a thrust (inferred feature *6* in Fig. 13A). The orientation of the curved folds is with consistent with left-slip shear along the fracture zone (feature *1* in Fig. 13A). The presence of likely drag folds (feature *7* in Fig. 13A) and oblique folds next to the fracture zone (feature *8* in Fig. 13A) are consistent with this interpretation.

The flanking ridges along the fracture labeled as feature 14b in Fig. 2A (also see shaded area labeled as feature *9* in Fig. 13B) are locally superposed by *en echelon* rounded-top ridges (feature *3* in Fig. 13B) interpreted as folds. The fold orientation requires left-slip motion along the fault labeled as feature *14b* in Fig. 2A and feature *1* (also shown as fracture A) in Fig. 13B. Widely spaced (>1 km) parallel fractures (feature 4 in Fig. 13B) cut across a flanking ridge of fracture A. As indicated by the consistent offset of features *5*, *6*, *7* and *8* in Fig. 13B, we interpret these fractures to be left-slip and represent synthetic *P*-shears (e.g., Sylvester, 1988) in a left-slip shear zone.

The anti-saturnian end of the Baghdad fracture zone consists of multiple strands that form a duplex-like structure (feature *15* in Fig. 2A and feature *2* in Fig. 13C). The most dominant strand is

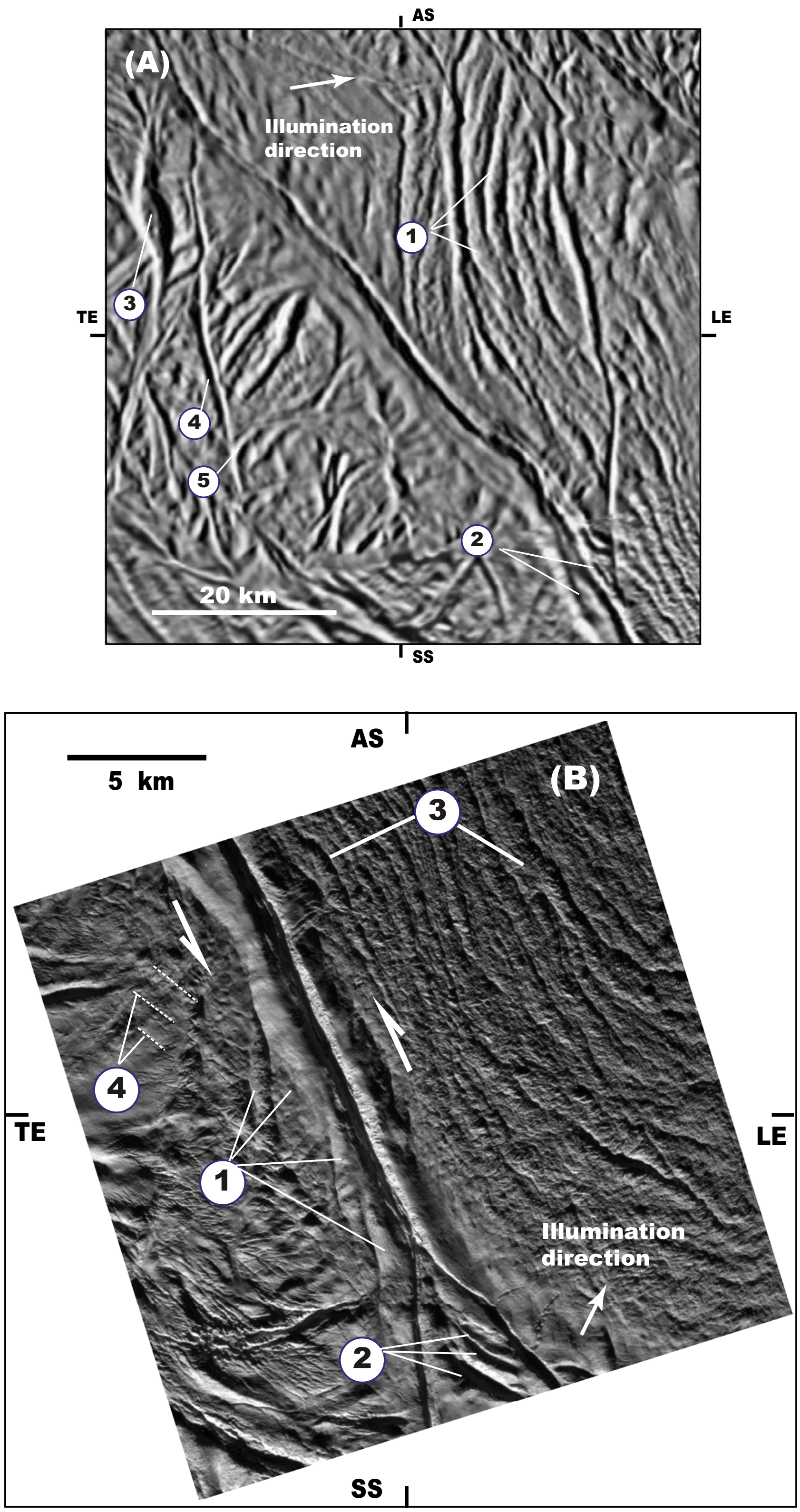

Fig. 14. (A) Oblique folds and oroclinal drag folds against the Damascus fracture zone. See Fig. 1B for location. (B) Oblique folds branching off from and *en echelon* extensional fractures located within the Damascus fracture zone. See Fig. 1B for location.

marked by a deep fissure (feature *1* in Fig. 13C) and the rest are characterized by shallower depressions (feature *2* in Fig. 13C). The above fractures either merge at both ends of the main Baghdad fracture trace (feature *2* in Fig. 13C) or branch off from the Baghdad fracture such as features *3*, *6*, and *9* in Fig. 13C. Additionally, some linear troughs parallel to the Baghdad fracture (feature *5* in Fig. 13C) are cut by perpendicularly oriented ridges and troughs (feature 4 in Fig. 13C) that are linked with the

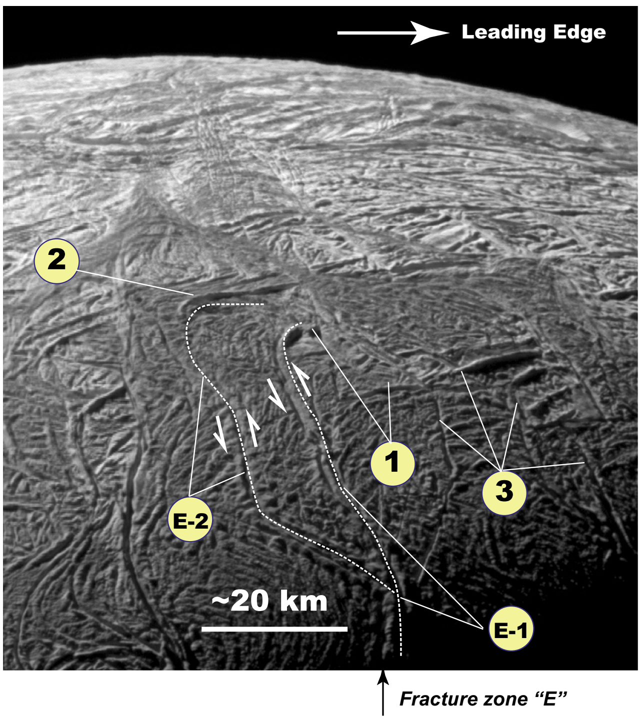

Fig. 15. Oblique view of fracture zone "E" and its relationship to its transverse termination structures marked by rounded-top ridges (e.g., feature 2). Numbers 1–3 and letters E-1 and E-2 are features discussed in the text. See Fig. 1A for viewing direction of the image.

Baghdad fractures. Because feature 5 in Fig. 13 is linked with the main trunk of the Baghdad fracture, we interpret it to have formed during the early stage of the tiger-stripe fracture-zone development.

The deep fissures along the Baghdad fracture zone and the orthogonally oriented termination structures may be explained by coeval extension in two perpendicular directions, but such a stress field is inconsistent with the orientation of folds linking with and trending obliquely to the fracture zone (features *6* and *7* in Fig. 13C). The oblique fold orientation (features *6* and *7* in Fig. 13C) requires the Baghdad fracture zone to be a left-slip structure, which is consistent with the shape of the oroclinal folds (features 8, 9 and 10 in Fig. 13C) and explains the presence of perpendicularly oriented highland strips (e.g., the region between two fractures labeled as feature 4 in Fig. 13C) as a result of horizontal shortening due to termination of the tiger-stripe fracture.

5.4. Damascus fracture zone

The anti-saturnian end of the Damascus fracture zone terminates at multiple zones of hook-shaped troughs and ridges (location 6 in Fig. 2A), whereas the sub-saturnian end of the fracture zone terminates at a horsetail fault system (location 7 in Fig. 2A). The fracture zone is a left-slip structure indicated by the following observations. Across its central segment, the fracture zone bounds ridges with rounded tops and oblique orientation to the main Damascus fracture zone (feature *1* in Fig. 14A); the oblique ridges are interpreted as folds. The orientation of the oblique folds and oroclinal-fold traces, expressed by the progressive rotation of the ridge trends into parallelism with the fracture zone, indicate TSF-parallel left-slip shear. The presence of a restraining bend (feature *2* in Fig. 14A), an obliquely oriented pop-up structure (feature *3* in Fig. 14A), and a left-slip branching fault (feature *4* in Fig. 14A) associated with a drag fold (feature *5* in Fig. 14A) indicates left-slip motion on the Damascus fracture zone. Left-slip faulting along the Damascus fracture zone is also indicated by *en echelon* folds branching off from the main fracture (feature *1* in Fig. 14B), *en echelon* extensional fractures in the Damascus fracture zone (feature *2* in Fig. 14B), and asymmetric drag folds in map view (feature *3* in Fig. 14B) against the fracture zone. Also note that a set of linear extensional cracks is developed on the TEM side of the Damascus fracture zone (feature *4* in Fig. 14B). Their orientation is consistent with left-slip faulting along the Damascus fracture zone.

5.5. Fracture zone "E"

Because plume eruption and IR-dark flanks have not been observed there, fracture zone "E" was not considered as one of the originally defined TSF (Porco et al., 2006, 2014). However, its structural trend, morphology, and termination structures are all similar to those of the early named TSF (Fig. 2). It is parallel to other TSF and has a similar spacing and length to the neighboring TSF; it is defined by a linear trough bounded by flanking ridges; and it terminates at hook-shaped trough-ridge zones (features *E-1* and *E-2* in Fig. 2A) and horsetail fault systems (feature *9* in

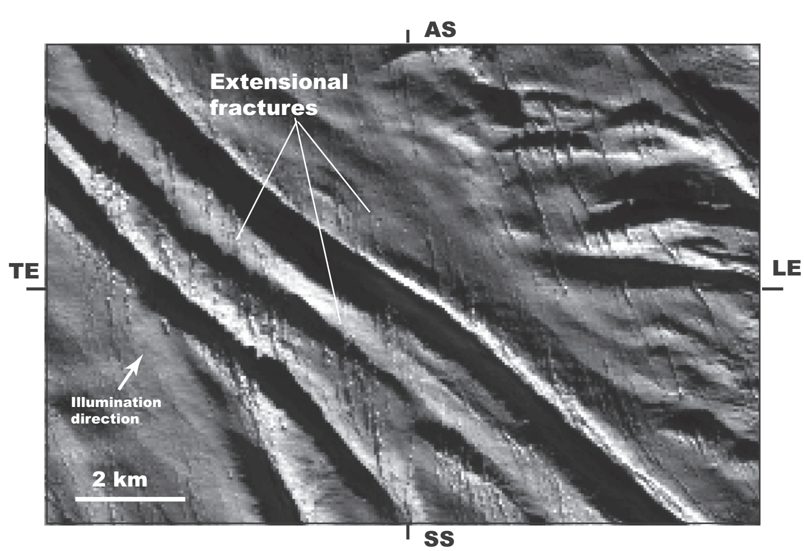

Fig. 16. Extensional fractures expressed as narrow linear grooves cut across tiger-stripe fracture "E". See Fig. 1A for location.

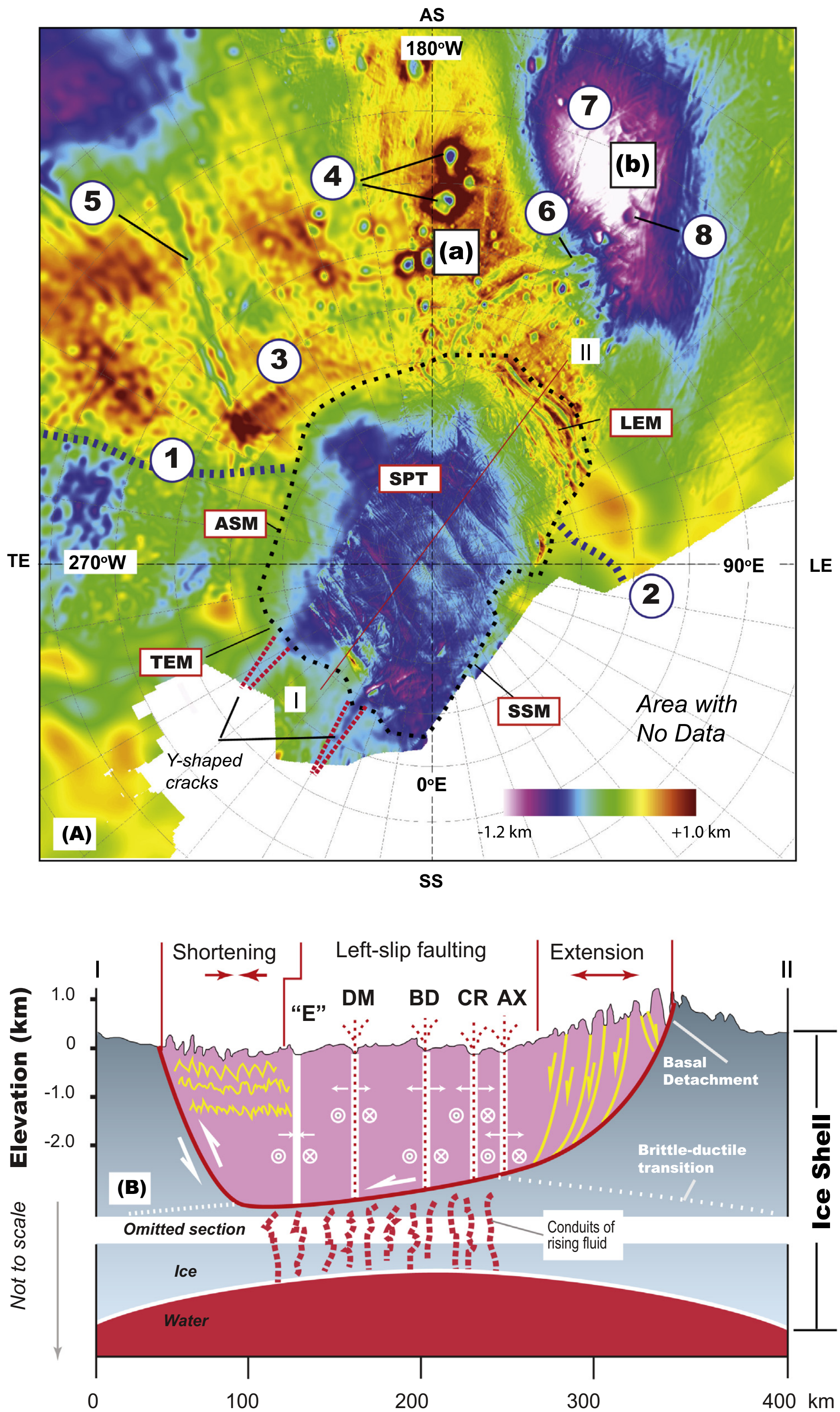

Fig. 17. (A) Digital topographic map of the South Polar Terrain (SPT) from Schenk and McKinnon (2009). Numbers refer to topographic features discussed in the text. Feature (a) is a highland region on the anti-saturnian side of the SPT, whereas feature (b) is a deep basin marked by ancient craters in the interior and cut by younger fracture zones expressed by troughs across its edge. See text for detailed discussion. Note that the spatial resolution of the topographic map varies. The thick dashed lines associated with (1) and (2) demarcate a pre-existing boundary between a highland region and a lowland region. Line I–II marks the location of the cross section in (B). (B) Topographic profile across the SPT from the LEM to the TEM. The line is drawn nearly perpendicular to the strike of the tiger-stripe fractures (TSF). Also shown are interpreted geologic structures in cross section view across the South Polar Terrain. The inferred detachment soles into the brittle-ductile transition zone in the ice shell.

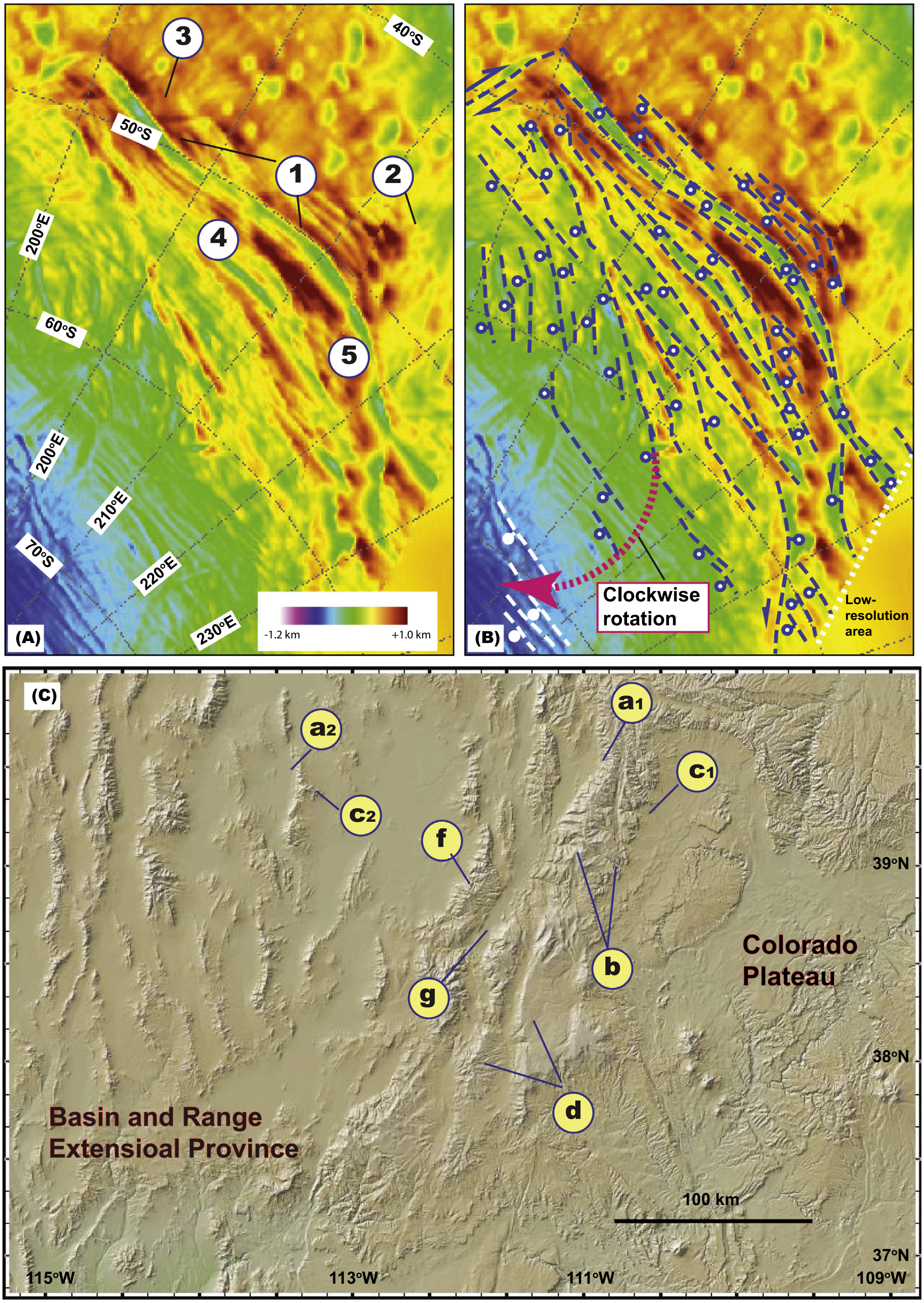

Fig. 18. (A) Digital topographic map across the LEM of the SPT from Schenk and McKinnon (2009). Numbers refer to topographic features discussed in the text. (B) Interpreted structural map across the LEM, based on results of kinematic analysis of Cassini images from the same area. Red dashed arrow indicates the direction of rotation of the SPT interior relative to its surrounding regions. Small circles against the fault traces are on the inferred hanging wall sides of the normal faults. (C) Topography of the transition zone between the active Basin and Range Extensional Province (west) and the stable Colorado plateau (east) in the western United States. The map was obtained using on-line software developed by GeoMapApp.org. (For interpretation of the references to color in this figure legend, the reader is referred to the web version of this article.)

Fig. 2A). The geometric and topographic relationships among fracture zone "E" and its termination structures are well illustrated by an oblique image of Enceladus shown in Fig. 15. In this image, fracture zone "E" splits into two branches toward the ASM, labeled as features *E-1* and *E-2* in Fig. 15. Both branches of the fracture zone terminate at hook-shaped folds with raised topography (features *1* and *2* in Fig. 15), which supports the contractional origin of the hook-shaped ridges. The "E" fractures and hook-shaped fold belts together display an L-shaped structural pattern in map view. Similar L-shaped structures (feature 3 in Fig. 15) also occur adjacent to fracture zone "E". The contractional origin of the termination structures implies left-slip motion on fracture zone "E". Fracture zone "E" is cut by younger extensional fractures (Fig. 16), which indicates that it has not been active very recently.

6. SPT topography

Schenk and McKinnon (2009) constructed digital topographic models covering ~50% of Enceladus' surface. Using their data we examine the relationship between the cratered terrains and the SPT and the relationship between topography and TSF kinematics. The SPT is bounded by a highland in the anti-saturnian direction and a lowland region in the sub-saturnian direction (Fig. 17A). The boundary between two regions (features *1* and *2* in Fig. 17A) is truncated by the SPT margin (feature *3* in Fig. 17A). The highland is ~1 km above the mean elevation and its surface is marked by craters (feature 4 in Fig. 17A) and troughs (features *5* and *6* in Fig. 17A). Nahm and Kattenhorn (2015) classified these structures as chasmata.

The SPT has the highest elevation along the LEM, sloping toward the TEM (Fig. 17A and B). The SSM is also higher than the ASM margin, creating a minor tilt of the SPT floor. Narrow ridges with a relief of 100–200 m are exclusively associated with the TSF (see topographic profile shown in Fig. 17B). Digital topography indicates that the LEM zone is dominated by extensional faults, as its morphology is remarkably similar to that of the Basin and Range province in the western United States (Fig. 18). Specifically, the troughs in the LEM are bounded by ridges with sharp and linear edges, which are interpreted as fault traces (compare features *1* in Fig. 18A with features *a1* and *a2* in Fig. 18C).

In a normal-fault-bounded crustal block on Earth, the block tilts in the opposite direction of the fault dip (feature *b* in Fig. 18C), which is expressed by a long and gentle slope from the crest line that lies closer to the fault-controlled scarp to the west. The tilted block is generally expressed by a long and gentle slope in contrast to the short and steep frontal slope along the fault trace (feature *d* in Fig. 18C). The back slope also commonly displays an irregular trace (features *c1* and *c2* in Fig. 18C), which differs from the linear fault trace (features *a1* and *a2* in Fig. 18C).

Fig. 18B is an interpreted structural map across the LEM, which shows that the width and number of full and half grabens, and thus the extensional strain, increase toward the sub-saturnian direction. This in turn requires clockwise rotation of the SPT interior relative to the cratered terrains (Fig. 18B).

The trough morphology of the TSF is best expressed along the Alexandria, Cairo, and Baghdad fracture zones, well developed along a segment of fracture zone "E", but is absent along the Damascus fracture zone (Fig. 19C). The absence of trough morphology along the Damascus fracture may result from a lower resolution of the topographic model and/or a narrower width of the trough zone than other TSF.

All the TSF display right-step bends (features *1–5* in Fig. 19A). As the TSF are inferred to be left-slip structures based on structural analysis, the right-step bends should be associated with transpressional deformation and high topography. This is indeed the case (Fig. 19A). The preferential occurrence of high topography on the trailing-edge side of the restraining bends along all the TSF is striking, which requires the bounding restraining-bend fault segments to dip toward the TEM direction. The consistent right-step-bend geometry and the TEM-ward dip direction require that their development was generated by a coherent stress field inducing left-slip shear. The flanking ridges and high topography along these bends may have been generated by transpression. Specifically, the associated deformation may have been associated with folding that has created broad and round-topped ridges that flank the TSF.

The erupting jets detected so far are all plotted on the TSF (Porco et al., 2014) (Fig. 19C). One may expect that the plumes occur along the strike-slip and transtensional segments of the faults, avoiding the transpressional segments. This is clearly not the case, as plumes are distributed along the entire traces of the TSF (Fig. 19C). This observation requires additional factors that control the locations and flux rates of the erupting plumes (Nimmo et al., 2014). The number of detected plumes along the TSF varies systematically, with most jets erupting along the Baghdad fracture zone located in the center of the SPT (Fig. 19D) (Porco et al., 2014).

7. Discussion

7.1. Main findings and their implications for the existing models

The main findings of this study are summarized below:

(1) The four segments of the semi-square-shaped SPT margin represent zones of contraction, extension, right-slip shear, and left-slip shear. Their kinematics requires the SPT to have moved from the LEM to the TEM. This transport direction is parallel to the regional topographic slope immediately outside the SPT.
(2) The ASM and SSM developed coevally with the formation of C-shaped extensional fractures, whereas the TEM developed coevally with the formation of the Y-shaped fractures (Fig. 1A).
(3) The TSF are left-slip structures displaying right-step restraining bends and terminating at hook-shaped fold zones or horsetail fault systems (see interpreted map in Fig. 1B).
(4) Locations of the erupting plumes along the TSF are independent of the detailed structural settings (e.g., transtensional or transpressional). This observation implies that the plume locations are unlikely to be controlled by long-term deformation processes expressed by left-slip motion along the TSF. Additional factors must be considered. For example, the eruption centers may be deeply buried pluton-like bodies and their distributions are controlled by Rayleigh–Taylor instability, similar to those along the fast-spreading mid-ocean ridges on Earth (Schouten et al., 1985; Carbotte et al., 2015).
(5) Segments of the TSF were locally reactivated or cut by extensional fractures (e.g., the anti-saturnian segment of the Cairo fracture zone; see Fig. 12A), suggesting that a young stress regime replaced the older stress regime responsible for initiating and maintaining left-slip motion along the TSF.

The existing literature regards the entire SPT margin as a zone of contractional deformation (e.g., Spencer and Nimmo, 2013), which is inconsistent with the results of this work (Fig. 2B). The varying kinematics of the SPT marginal zone is also inconsistent with SPT formation by domal uplift (e.g., Gioia et al., 2007; Crow-Willard and Pappalardo, 2015), which requires the formation of

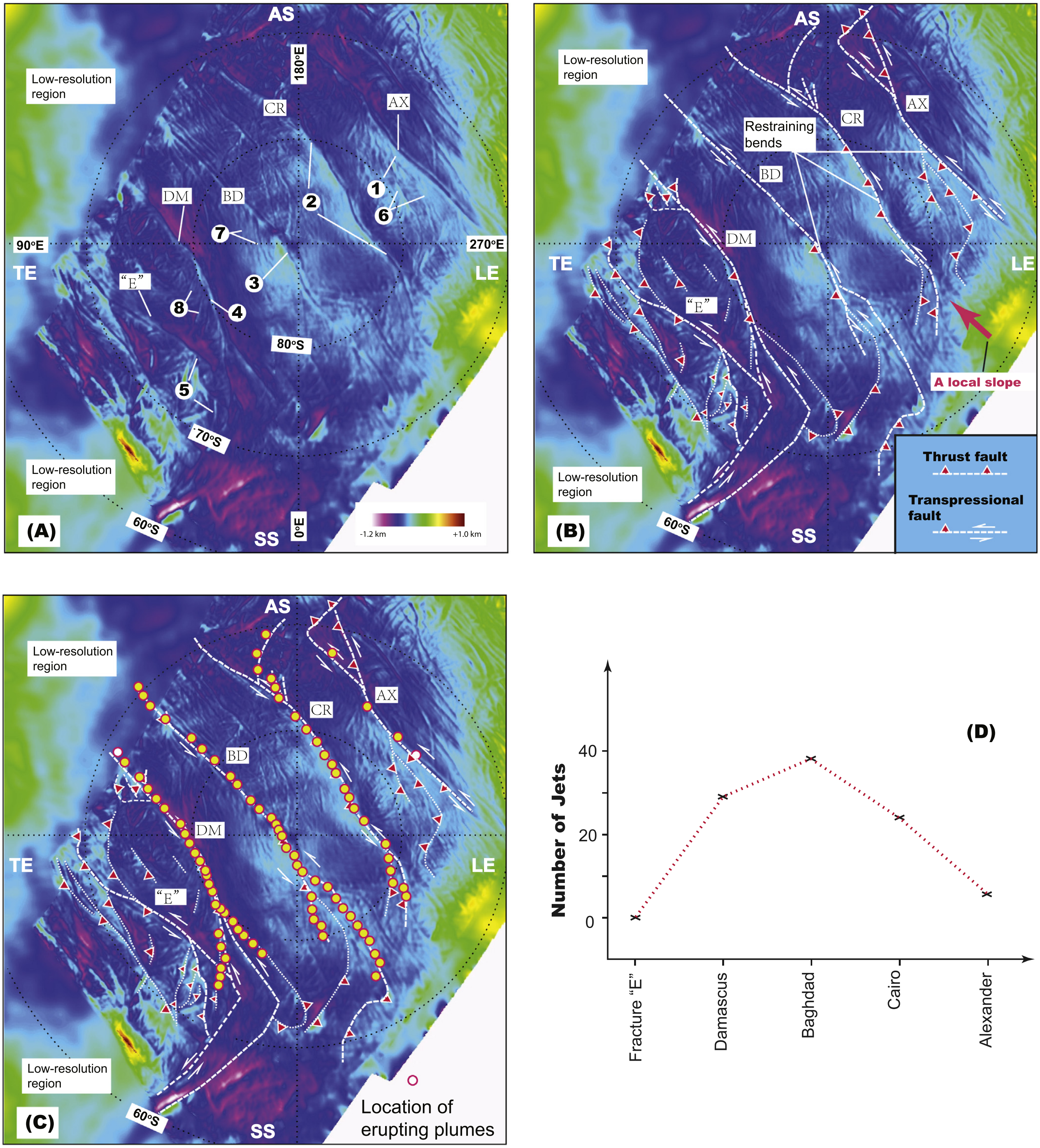

Fig. 19. (A) Digital topographic map of the SPT interior from Schenk and McKinnon (2009). Numbers refer to topographic features discussed in the text. (B) The traces of the TSF and interpreted fault kinematics. Red triangles are on the inferred hanging walls of the transpressional segments of the left-slip faults. Red arrow points to a local slope direction. (C) Locations of erupting water–ice jets from Porco et al. (2014) along the TSF. (D) Spatial variation of the number of erupting jets along the TSF as a function of location. Data are from Porco et al. (2014). Note that the number of the jets is the highest along the Baghdad fracture zone in the central SPT. (For interpretation of the references to color in this figure legend, the reader is referred to the web version of this article.)

axially symmetric structures across the SPT and its margin that are not observed. Strike-slip faulting with alternating senses of motion (Nimmo et al., 2007; Smith-Konter and Pappalardo, 2008) must have been ineffective in creating observable structures, as our mapping does not reveal mutually cross-cutting structures indicating opposite senses of strike-slip motion along the TSF. Asymmetric topography (Figs. 17 and 19) across each of the five TSF is also inconsistent with their being mid-ocean-ridge-like spreading centers (Helfenstein et al., 2008).

A tensile-fracture origin for TSF initiation (e.g., Porco et al., 2006) is inconsistent with our observations for the following reasons. (1) The inferred stress field would have initiated not only the TSF but also parallel extensional fractures nearby, which are not observed. Instead, folds are the most dominant features adjacent to the TSF. (2) An extensional origin for the TSF would require a change in stress state from TSF-normal extension to TSF-parallel left-slip faulting, which in turn would have created a detectable cross-cutting relationship that is not observed. (3) TSF-perpendicular extension is kinematically incompatible with extension along the LEM and contraction along the TEM, as it would require contraction along the two margins parallel to the TSF.

7.2. Ice-shell strength and stress induced by ice-shell thickness variation

Based on the constructed digital topographic models, Schenk and McKinnon (2009) recognized several large depressions on Enceladus, which are 90–175 km across and 800–1500 m deep. Considering the lack of large impact-related features on Enceladus, the depressions may have originated through tectonic or thermally induced convective processes, with topography supported mostly by Airy isostasy (i.e., the effective elastic thickness of the ice shell is nearly zero) (Schenk and McKinnon, 2009; Besserer et al., 2013). This inference is consistent with inversion of gravity data and modeling results of flexurally supported topography, which show that the maximum elastic thickness of the SPT must be less than 0.5 km (Giese et al., 2008; Bland et al., 2012; Iess et al., 2014). The large variation of surface topography under Airy isostasy requires large lateral variation of ice-shell thickness, which in turn requires the presence of deviatoric stress in the ice shell. The magnitude of the deviatoric stress may be estimated as follows. The present-day elevation difference between the highland and lowland regions immediately outside the South Polar Terrain is 0.5–1.0 km, which yields a 8.5–17 km difference in ice-shell thickness assuming Airy isostasy and using nominal ice-shell (934 kg/m^3) and water (1000 kg/m^3) densities. This thickness difference can generate a shear stress on the order of 0.06–0.13 MPa, which is the product of the density contrast between ice and water ($\Delta\rho$), ice-shell thickness difference (Δh = 8.5–17 km), and the surface gravitational acceleration of Enceladus (0.114 m/s^2) (e.g., Nimmo and Manga, 2009). This estimated differential stress in the ice shell is similar in magnitude to the estimated diurnal tidal stress (Nimmo et al., 2007). Note that the use of the phrase "ice shell" does not imply the existence of a global ocean on Enceladus. It simply refers to the uppermost ice layer, consisting of a brittle upper layer and a ductile lower layer, in the south-polar region where a local sea has been well established (see review by Spencer and Nimmo, 2013).

Like the silicate crust on Earth, the strength of the ice shell is controlled by Amontons' Law in the upper section (e.g., Schulson, 2002) and ductile creep in the lower section (Goldsby and Kohlstedt, 2001); the two regions are separated by the brittle ductile transition whose depth varies laterally depending on the local vertical thermal gradient assuming a spatially uniform strain rate. The estimated differential stress (i.e., 2 × maximum shear stress) may drive ice-shell deformation when it exceeds the average strength of the ice shell, which is an integration of the brittle and ductile strength with depth averaged by the ice-shell thickness. Considering the many uncertainties in ice rheology on Enceladus (e.g., Goldsby and Kohlstedt, 2001; Schulson and Fortt, 2013), we make no attempt to conduct quantitative estimates on the onset of the deformation, but we simply point out that the average strength of the ice shell decreases when it heats up, as this would reduce the average strength of the ductile section of the ice shell. Based on this simple physics, we envision that a transient thermal event below regions with large crustal-thickness variation could lead to lateral spreading of the thick ice shell. Indeed, thermally induced viscous flow on Enceladus has long been noted as a mechanism to explain the morphology (Smith et al., 1981; Bland et al., 2012) and size distribution (Kirchoff and Schenk, 2009) of craters on Enceladus. The combined effect of topography-induced stress and thermally induced viscosity reduction leading to lateral spreading is a major process in the evolution of Earth's continental lithosphere. The mid-Tertiary collapse of the North American Cordilleran orogen during slab rollback and its induced mantle upwelling (Coney, 1987; Liu and Shen, 1998) and Cenozoic trench-ward gravitational spreading of the Tibetan plateau and east Asia initiated by mantle heating (England and Houseman, 1989; Yin, 2010) are some of the best examples of this process. Our proposed mechanism implies that the diurnal tidal stress may be a secondary controlling factor in driving the tectonic deformation of the South Polar Terrain on Enceladus, as the surface geology of the SPT does not support bi-directional strike-slip movement on any of the TSF.

7.3. Tectonic model for the evolution of the South Polar Terrain

Here, we propose a tectonic model that explicitly explains (1) the structural relationship between the SPT marginal zone and TSF, (2) the observed kinematics of the two structural systems, and (3) the topography relationship across the SPT and its surrounding regions (Fig. 20). In map view, extension along the LEM resulted in the SPT as a deformable viscous sheet toward the TEM (Fig. 20A). SPT motion was accommodated by right-slip and left-slip motion along the ASM and SSM. Respectively, and shortening across the TEM (Fig. 20A). The SSM-ward increase in extension along the LEM and the SSM-ward increase in shortening along the TEM created distributed right-slip shear across the *interior* of the entire moving SPT, which initiated folds (i.e., the closely spaced folds between the tiger-stripe fractures; see Barr and Preuss, 2010) and later left-slip faults (i.e., the tiger-stripe fracture zones); the folds and the left-slip faults were oriented obliquely to the regional right-slip shear direction in a simple-shear flow (e.g., Sylvester, 1988). The regional right-slip shear across the SPT interior was not only responsible for creating the left-slip tiger-stripe faults but was also responsible for their subsequent rotation through bookshelf faulting (i.e., left-slip faulting along the TSF accommodated regional right-slip shear across the SPT interior). The angle between the shear-failure planes and the maximum compressive stress direction is assumed to be 30°, representing well an average coefficient of internal friction of ~0.6 for ice (Schulson, 2001) (Fig. 20A–C). In this model the development of the right-step restraining bends on the TSF results from linking *en echelon* left-slip faults (Fig. 20C and D). Although the stress state is only shown in Fig. 20A, we infer that this same stress regime has persisted in all the stages of the SPT development and drove the regional right-slip shear deformation across the interior of the SPT.

We hypothesize that the initiation of viscous flow across the SPT was triggered by a transient heating event from below, which could have been induced by a rising plume, tidal heating, convection of warm ice, and/or coupling and feedbacks between the above processes (Nimmo and Pappalardo, 2006; Barr and McKinnon, 2007; Tobie et al., 2008; Běhounková et al., 2012, 2013; Shoji et al., 2014) (Fig. 20E). The heating event drastically reduced the ice-shell viscosity, allowing unidirectional viscous flow of the ice shell along the direction of the maximum pressure gradient induced by ice-shell-thickness variation.

A transient heating event must be localized in the SPT. We note that the region between the cratered highland (feature *a* in Fig. 17A) and a deep basin (feature b in Fig. 17A) on the leading-edge side of the SPT has a topographic relief of >2 km. Our own preliminary examination of the areas indicates a lack of recent tectonic deformation (Fig. 17A; also see Fig. 1 in Spencer and Nimmo, 2013). The high topography region also has no active plumes nor

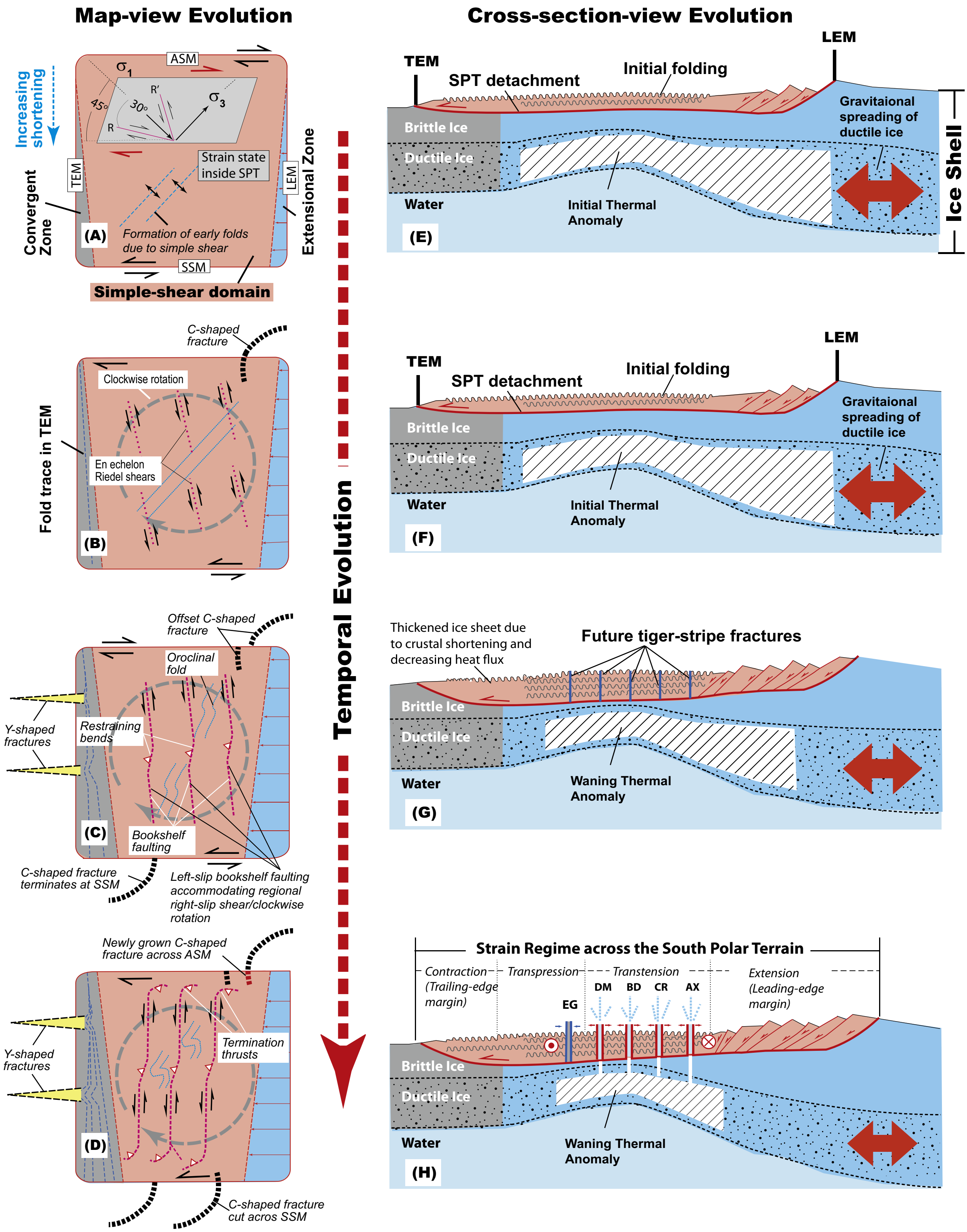

Fig. 20. Tectonic model for the evolution of the South Polar Terrain (SPT). (A) Non-uniform extension and shortening along the LEM and TEM created simple shear. R and R′: Riedel and conjugate Riedel shears; σ1 and σ3: maximum and minimum principal stresses. (B) Formation of *en echelon* left-slip fractures under simple shear. (C) Linking *en echelon* fractures led to formation of through-going left-slip faults and right-step restraining bends. Left-slip faults and folds also rotate clockwise under simple shear. (D) Left-slip faults terminate at contractional structures and continue to rotate. (E) Preexisting plateau created a pressure gradient in the viscous ice shell. (F) Rising warm plume caused crustal thinning, viscosity reduction, lateral flow of the ice shell, and closely spaced folding above a shallow decollement. (G) Left-slip faulting replaced folding to accommodate distributed simple shear across the SPT. (H) Strain state is extensional and transtensional in the upslope SPT, whereas strain is contractional and transtensional in the downslope SPT.

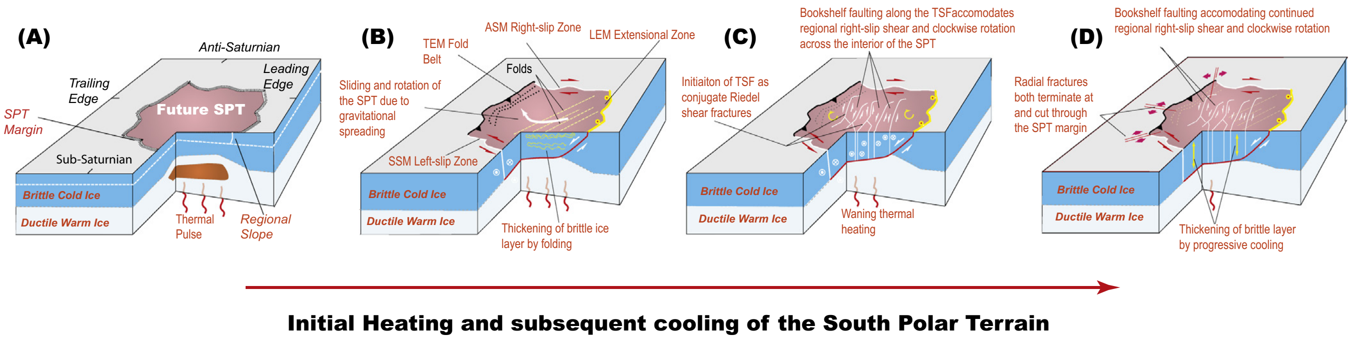

Fig. 21. A three-dimensional block diagram for the evolution of the South Polar Terrain. (A) The region had a regional slope from the leading-edge to the trailing-edge direction as a result of thinning of the ice shell toward the trailing-edge direction. A transient thermal event was induced possibly by tidal heating in the ductile warm ice. (B) Heating from below caused a drastic reduction of ice-shell viscosity, which in turn induced trailing-edge-ward spreading of the viscous ice shell. The initial spreading induced closely spaced folds across the interior of the SPT as a result of a thin brittle ice shell that favors buckling rather than faulting. (C) As the brittle ice layer becomes thicker due to gradual cooling of the SPT, brittle faulting became a favored mode of deformation to accommodate internal deformation of the SPT during its translation and rotation. The clockwise rotation was driven by differential extension along the leading-edge margin of the SPT that led to the formation of the tiger-stripe fractures as conjugate Riedel shear fractures. The clockwise rotation in turn was accommodated by left-slip bookshelf faulting along the tiger-stripe fractures that rotate in a clockwise sense. (D) Continued compression along the trailing-edge margin of the SPT caused the formation of extensional fracture systems radial to this arcuate segment of the SPT margin.

high thermal emission (Porco et al., 2006), implying that its ice shell is relatively cold and thus its averaged viscosity is higher than that of the SPT ice shell. The above observations together suggest that the strength of a relatively cold portion of the ice shell on Enceladus is capable of sustaining extreme topographic relief (>2 km) over 1–4 byr, consistent with inferences by Kirchoff and Schenk (2009) and Bland et al. (2012).

Owing to the initially high heat flux of the inferred transient heating event, the ice shell of the SPT was dominated by early shallow detachment faulting and closely spaced folding (Fig. 20E and F), followed by deep detachment faulting and widely spaced fracturing as a result of increasing ice-shell thickness and decreasing heat flux (Fig. 20G). Widely spaced fracturing in turn created the tiger-stripe shear zones. The basal sliding surface of the detachment fault most likely follows the brittle ductile transition zone, similar to the detachment faults on Earth (e.g., Yin, 1989; Lister and Davis, 1989; Yin and Dunn, 1992). As shown in Fig. 17A, a regional slope exists across the interior of the SPT from the LEM toward the TEM. During gravitational spreading, the strain state in the ice shell should be extensional in the upslope section of the SPT interior toward the LEM and contractional in the downslope section of the SPT interior toward the TEM (Fig. 20H). This scenario is consistent with the preferential occurrence of plume eruptions on four of the five TSF in the upslope direction across the SPT interior toward the LEM (Porco et al., 2014).

In the context of our kinematic model, the coeval development of the Y-shaped fractures (Fig. 20C and D) can be understood, as they are concentrated along the axial traces of the arcuate fold belts where arc-parallel extension is expected. However, the mechanical relationship between motion on the ASM and SSM and the coeval but episodic development of the C-shaped fractures is not clear. It is possible that the development of the C-shaped fractures in the ancient cratered terrains was driven by a different mechanism such as tidal stress rather than by gravitational spreading within the SPT. In fact, tidal stress may have caused reactivation and lengthening of preexisting fractures as envisioned for the development of a segment of the Cairo fracture zone (Fig. 12E). A three-dimensional evolutionary model of the South Polar Terrain is shown in Fig. 21.

8. Conclusions

In this study we show via systematic mapping and detailed structural analysis that the semi-squared South Polar Terrain (SPT) is bounded by a right-slip shear zone and a left-slip shear zone along the anti-saturnian and sub-saturnian margins and an extensional fault zone and a contractional fold zone along the leading-edge and trailing-edge margins of the SPT. Motion on the boundary zone accommodates lateral translation of the SPT as a single ice sheet with the transport direction from topographically high to topographically low regions. The correlation of regional topography and inferred transport direction implies that the gradient of gravitational potential energy has been the main driving mechanism for the tectonic development of the SPT. In map view, the SPT deformation is characterized by distributed right-slip shear parallel to the SPT transport direction. This regional shear is induced by non-uniform extension and contraction along the leading- and trailing-edge margins of the SPT. The regional right-slip shear across the SPT was responsible for initiating (1) the five parallel tiger-stripe fractures (TSF) as left-slip conjugate Riedel shears and (2) the closely spaced folds in the TSF-bounded panels. Subsequent left-slip bookshelf faulting along the parallel tiger-stripe fractures accommodates the continued regional right-slip shear and the induced clockwise rotation across the SPT. We suggest that, to the first approximation, the inferred flow-like tectonics across the SPT on Enceladus is best explained by the occurrence of a transient thermal event centered near the south pole (see more details below). The thermal event increased the ice-shell temperature of the SPT, which in turn lowered the ice-shell viscosity and allowed the release of gravitational potential energy via lateral viscous flow within the ice shell with variable thickness. Although the long-term gravitational spreading has controlled the overall tectonic pattern and evolution of the SPT, the tidal stress must have assisted the diurnal opening and closing of the TSF and thus modulate the temporal variation of plume fluxes (Nimmo et al., 2014). The tidal stress may have also modified the fracture patterns across the SPT while reactivating and lengthening the preexisting weakness.

Acknowledgments

We thank Paul Schenk for making the digital topographic data available and Jennifer Scully for generating the color displays of the topographic data. We thank Paul Helfenstein for his constructive review. His pioneering work and thought-provoking models for the tectonic development of Enceladus were the foundation and motivation for the work presented in this study. We are also very grateful for a superb review by Amanda Nahm, which led to clarification and significant improvement of the original manuscript. Work by RTP was carried out at the Jet Propulsion

Laboratory, California Institute of Technology, under a contract with the National Aeronautics and Space Administration. AY's work on the mechanics and kinematics of strike-slip faults was supported by a grant from the Tectonics Program of the U.S. National Science Foundation.

References

Anderson, E.M., 1942. The Dynamics of Faulting and Dyke Formation with Applications to Britain. Oliver and Boyd, Edinburgh, 191pp.
Barr, A.C., 2008. Mobile lid convection beneath Enceladus' South Polar Terrain. J. Geophys. Res. 113, E07009.
Barr, A.C., McKinnon, W.B., 2007. Convection in Enceladus' ice shell: Conditions for initiation. Geophys. Res. Lett. 340, L09202.
Barr, A.C., Preuss, L.J., 2010. On the origin of south polar folds on Enceladus. Icarus 208 (1), 499–503.
Běhounková, M. et al., 2012. Tidally-induced melting events as the origin of south-pole activity on Enceladus. Icarus 219, 655–664.
Běhounková, M. et al., 2013. Impact of tidal heating on the onset of convection in Enceladus's ice shell. Icarus 226, 898–904.
Besserer, J. et al., 2013. Convection-driven compaction as a possible origin of Enceladus's long wavelength topography. J. Geophys. Res. 118, 1–8. http://dx.doi.org/10.1002/jgre.20079.
Bland, M.T. et al., 2012. Enceladus' extreme heat flux as revealed by its relaxed craters. Geophys. Res. Lett. 39, L17204.
Boyer, S.E., Elliott, D., 1982. Thrust systems. Am. Assoc. Petrol. Geol. 66, 1196–1230.
Burbank, D.W., Anderson, R.S., 2011. Tectonic Geomorphology. John Wiley & Sons.
Burchfiel, B.C. et al., 1989. Intracrustal detachment within zones of continental deformation. Geology 17 (8), 748–752.
Carbotte, S.M. et al., 2015. Tectonic and magmatic segmentation of the Global Ocean Ridge System: A synthesis of observations. Geol. Soc. Lond. Spec. Publ. 420, SP420–505.
Collins, G.C., Goodman, J.C., 2007. Enceladus' south polar sea. Icarus 189 (1), 72–82.
Coney, P.J., 1987. The regional tectonic setting and possible causes of Cenozoic extension in the North American Cordillera. Geol. Soc. Lond. Spec. Publ. 28 (1), 177–186.
Cooke, M.L., Underwood, C.A., 2001. Fracture termination and step-over at bedding interfaces due to frictional slip and interface opening. J. Struct. Geol. 23, 223–238.
Cowgill, E. et al., 2000. Is the North Altyn fault part of a strike-slip duplex along the Altyn Tagh fault system? Geology 28 (3), 255–258.
Cowgill, E. et al., 2004a. The Akato Tagh bend along the Altyn Tagh fault, northwest Tibet 1: Smoothing by vertical-axis rotation and the effect of topographic stresses on bend-flanking faults. Geol. Soc. Am. Bull. 116 (11–12), 1423–1442.
Cowgill, E. et al., 2004b. The Akato Tagh bend along the Altyn Tagh fault, northwest Tibet 2: Active deformation and the importance of transpression and strain hardening within the Altyn Tagh system. Geol. Soc. Am. Bull. 116 (11–12), 1443–1464.
Crow-Willard, E.N., Pappalardo, R.T., 2015. Structural mapping of Enceladus and implications for formation of tectonized regions. J. Geophys. Res.: Planets. http://dx.doi.org/10.1002/2015JE004818.
England, P., Houseman, G., 1989. Extension during continental convergence, with application to the Tibetan Plateau. J. Geophys. Res.: Solid Earth 94 (B12), 17561–17579.
Figueredo, P.H., Greeley, R., 2000. Geologic mapping of the northern leading hemisphere of Europa from Galileo solid-state imaging data. J. Geophys. Res.: Planets (1991–2012) 105 (E9), 22629–22646.
Giese, B. et al., 2008. Enceladus: An estimate of heat flux and lithospheric thickness from flexurally supported topography. Geophys. Res. Lett. 35 (24).
Gioia, G. et al., 2007. Unified model of tectonics and heat transport in a frigid Enceladus. Proc. Natl. Acad. Sci. USA 104, 13578–13581.
Goguen, J.D. et al., 2013. The temperature and width of an active fissure on Enceladus measured with Cassini VIMS during the 14 April 2012 south pole flyover. Icarus 226 (1), 1128–1137.
Goldsby, D.L., Kohlstedt, D.L., 2001. Superplastic deformation of ice: Experimental observations. J. Geophys. Res.: Solid Earth (1978–2012) 106 (B6), 11017–11030.
Han, L., Tobie, G., Showman, A.P., 2012. The impact of a weak south pole on thermal convection in Enceladus' ice shell. Icarus 218 (1), 320–330.
Hedman, M.M. et al., 2013. An observed correlation between plume activity and tidal stresses on Enceladus. Nature 500, 182–184.
Helfenstein, P. et al., 2006. Patterns of fracture and tectonic convergence near the south pole of Enceladus. Lunar Planet. Sci. 37. Abstract 2182.
Helfenstein, P. et al., 2008. Enceladus South Polar Terrain geology: New details from Cassini ISS high resolution imaging. American Geophysical Union (Fall). Abstract.
Howett, C.J.A. et al., 2010. Thermal inertia and bolometric Bond albedo values for Mimas, Enceladus, Tethys, Dione, Rhea and Iapetus as derived from Cassini/CIRS measurements. Icarus 206 (2), 573–593.
Hurford, T.A. et al., 2007. Eruptions arising from tidally controlled periodic openings of rifts on Enceladus. Nature 447, 292–294.
Iess, L. et al., 2014. The gravity field and interior structure of Enceladus. Science 344 (6179), 78–80.
Ingersoll, A.P., Pankine, A.A., 2010. Subsurface heat transfer on Enceladus: Conditions under which melting occurs. Icarus 206 (2), 594–607.
Jackson, J.A. et al., 1982. Seismicity, normal faulting, and the geomorphological development of the Gulf of Corinth (Greece): The Corinth earthquakes of February and March 1981. Earth Planet. Sci. Lett. 57 (2), 377–397.
Jackson, J.A. et al., 1988. Relations between normal-fault geometry, tilting and vertical motions in extensional terrains: An example from the southern Gulf of Suez. J. Struct. Geol. 10 (2), 155–170.
Kattenhorn, S.A., 2004. Strike-slip fault evolution on Europa: Evidence from tailcrack geometries. Icarus 172 (2), 582–602.
Kim, Y.-S., Sanderson, D.J., 2006. Structural similarity and variety at the tips in a wide range of strike-slip faults: A review. Terra Nova 18, 330–344.
Kirchoff, M.R., Schenk, P., 2009. Crater modification and geologic activity in Enceladus' heavily cratered plains: Evidence from the impact crater distribution. Icarus 202, 656–668.
Kohlstedt, D.L., Mackwell, S.J., 2010. Strength and deformation of planetary lithospheres. In: Watters, T.R., Schultz, R.A. (Eds.), Planetary Tectonics. Cambridge University Press, New York, pp. 397–456.
Lister, G.S., Davis, G.A., 1989. The origin of metamorphic core complexes and detachment faults formed during Tertiary continental extension in the northern Colorado River region, USA. J. Struct. Geol. 11, 65–94.
Lister, G.S., Etheridge, M.A., Symonds, P.A., 1986. Detachment faulting and the evolution of passive continental margins. Geology 14 (3), 246–250.
Liu, M., Shen, Y., 1998. Crustal collapse, mantle upwelling, and Cenozoic extension in the North American Cordillera. Tectonics 17 (2), 311–321.
Martens, H.R. et al., 2015. Spatial distribution of ice blocks on Enceladus and implications for their origin and emplacement. Icarus 245, 162–176.
Matsuyama, I., Nimmo, F., 2008. Tectonic patterns on reoriented and despun planetary bodies. Icarus 195, 459–473.
McKinnon, W.B., 2015. Effect of Enceladus's rapid synchronous spin on interpretation of Cassini gravity. Geophys. Res. Lett. 42, 2015G. http://dx.doi.org/10.1002/L063384.
Means, W.D., 1989. Stretching faults. Geol. 17 (10), 893–896.
Nahm, A.L., Kattenhorn, S.A., 2015. A unified nomenclature for tectonic structures on the surface of Enceladus. Icarus 2015. http://dx.doi.org/10.1016/j.icarus.2015.06.009.
Nimmo, F., Manga, M., 2009. Geodynamics of Europa's icy shell. In: Pappalardo, R.T., McKinnon, W.B., Khurana, K. (Eds.), Europa. The University of Arizona Press, Tucson, pp. 382–404.
Nimmo, F., Pappalardo, R.T., 2006. Diapir-induced reorientation of Saturn's moon Enceladus. Nature 441, 614–616.
Nimmo, F. et al., 2007. Shear heating as the origin of the plumes and heat flux on Enceladus. Nature 447, 289–291.
Nimmo, F., Porco, C., Mitchell, C., 2014. Tidally modulated eruptions on Enceladus: Cassini ISS observations and models. Astron. J. 148, 46.
Nye, J.F., 1952. The mechanics of glacier flow. J. Glaciol. 2 (12), 82–93.
O'Neill, C., Nimmo, F., 2010. The role of episodic overturn in generating the surface geology and heat flow on Enceladus. Nat. Geosci. 3 (2), 88–91.
Paranicas, C. et al., 2012. Energetic charged particle weathering of Saturn's inner satellites. Planet. Space Sci. 61 (1), 60–65.
Paterson, W.S.B., Cuffey, K.M., 1994. The Physics of Glaciers, vol. 3. Pergamon, Oxford.
Patthoff, D.A., Kattenhorn, S.A., 2011. A fracture history on Enceladus provides evidence for a global ocean. Geophys. Res. Lett. 38, L18201.
Pappalardo, R.T., Greeley, R., 1995. A review of the origins of subparallel ridges and troughs: Generalized morphological predictions from terrestrial models. J. Geophys. Res.: Planets (1991–2012) 100 (E9), 18985–19007.
Peltzer, G., Tapponnier, P., 1988. Formation and evolution of strike-slip faults, rifts, and basins during the India–Asia collision: An experimental approach. J. Geophys. Res.: Solid Earth (1978–2012) 93 (B12), 15085–15117.
Porco, C.C. et al., 2006. Cassini observes the active south pole of Enceladus. Science 311, 1393–1401.
Porco, C., DiNino, D., Nimmo, F., 2014. How the geysers, tidal stresses, and thermal emission across the South Polar Terrain of Enceladus are related. Astron. J. 148, 45.
Roberts, J.H., Nimmo, F., 2008. Tidal heating and the long-term stability of a subsurface ocean on Enceladus. Icarus 194 (2), 675–689.
Schenk, P.M., McKinnon, W.B., 2009. One-hundred-km-scale basins on Enceladus: Evidence for an active ice shell. Geophys. Res. Lett. 36, L16202.
Schenk, P., Schmidt, J., White, O., 2011a. The snows of Enceladus. EPSC-DPS Joint Meeting 2011, Nantes, France. Abstract #1358.
Schenk, P. et al., 2011b. Plasma, plumes and rings: Saturn system dynamics as recorded in global color patterns on its midsize icy satellites. Icarus 211 (1), 740–757.
Schouten, H., Klitgord, K.D., Whitehead, J.A., 1985. Segmentation of mid-ocean ridges. Nature 317 (6034), 225–229.
Schulson, E.M., 2001. Brittle failure of ice. Eng. Fract. Mech. 68, 1839–1887.
Schulson, E.M., 2002. Compressive shear faults in ice: Plastic vs. coulombic faults. Acta Mater. 50 (13), 3415–3424.
Schulson, E.M., Fortt, A.L., 2013. Static strengthening of frictional surfaces of ice. Acta Mater. 61 (5), 1616–1623.
Schultz, R.A. et al., 2010. Interpretation and analysis of planetary structures. J. Struct. Geol. 32 (6), 855–875.
Segall, P., Pollard, D.D., 1983. Joint formation in granitic rock of the Sierra Nevada. Geol. Soc. Am. Bull. 94 (5), 563–575.
Shoji, D. et al., 2014. Non-steady state tidal heating of Enceladus. Icarus 235, 75–85.
Sieveka, E.M., Johnson, R.E., 1982. Thermal-and plasma-induced molecular redistribution on the icy satellites. Icarus 51 (3), 528–548.

Smith, B.A. et al., 1981. Encounter with Saturn: Voyager 1 imaging science results. Science 212 (4491), 163–191.
Smith-Konter, B., Pappalardo, R.T., 2008. Tidally driven stress accumulation and shear failure of Enceladus's tiger stripes. Icarus 198, 435–451.
Spencer, J.R., Nimmo, F., 2013. Enceladus: An active ice world in the Saturn system. Annu. Rev. Earth Planet. Sci. 41, 693–717.
Spencer, J.R. et al., 2009. Enceladus: An active cryovolcanic satellite. In: Dougherty, M., Esposito, L., Krimigis, S. (Eds.), Saturn from Cassini–Huygens. Springer, Netherlands, pp. 683–724.
Spencer, J.R. et al., 2013. Enceladus heat flow from high spatial resolution thermal emission observations. EPSC Abstracts, 8.
Suppe, J., 1983. Geometry and kinematics of fault-bend folding. Am. J. Sci. 283 (7), 684–721.
Swanson, M.T., 1988. Pseudotachylyte-bearing strike-slip duplex structures in the Fort Foster Brittle Zone, S. Maine. J. Struct. Geol. 10 (8), 813–828.
Sylvester, A.G., 1988. Strike-slip faults. Geol. Soc. Am. Bull. 100 (11), 1666–1703.
Taylor, M., Yin, A., 2009. Active structures of the Himalayan–Tibetan orogen and their relationships to earthquake distribution, contemporary strain field, and Cenozoic volcanism. Geosphere 5 (3), 199–214.
Taylor, M. et al., 2003. Conjugate strike-slip faulting along the Bangong-Nujiang suture zone accommodates coeval east–west extension and north–south shortening in the interior of the Tibetan Plateau. Tectonics 22 (4), 1044. http://dx.doi.org/10.1029/2002TC001361.
Thomas, P.C. et al., 2015. A global subsurface ocean on Enceladus indicated by measured physical libration. Sci. Adv., submitted for publication
Tobie, G., Čadek, O., Sotin, C., 2008. Solid tidal friction above a liquid water reservoir as the origin of the south pole hotspot on Enceladus. Icarus 196, 642–652.
Travis, B.J., Schubert, G., 2015. Keeping Enceladus warm. Icarus 250, 32–42.
Walker, R., Jackson, J., Baker, C., 2003. Surface expression of thrust faulting in eastern Iran: Source parameters and surface deformation of the 1978 Tabas and 1968 Ferdows earthquake sequences. Geophys. J. Int. 152 (3), 749–765.
Walker, C.C., Bassis, J.N., Liemohn, M.W., 2012. On the application of simple rift basin models to the south polar region of Enceladus. J. Geophys. Res.: Planets (1991–2012) 117 (E7).
Watters, T.R. et al., 2010. Evidence of recent thrust faulting on the Moon revealed by the Lunar Reconnaissance Orbiter Camera. Science 329 (5994), 936–940.
Willemse, E.J., Peacock, D.C., Aydin, A., 1997. Nucleation and growth of strike-slip faults in limestones from Somerset, UK. J. Struct. Geol. 19 (12), 1461–1477.
Woodcock, N.H., Fischer, M., 1986. Strike-slip duplexes. J. Struct. Geol. 8 (7), 725–735.
Yeats, R.S. et al., 1997. The Geology of Earthquakes, vol. 568. Oxford University Press, New York.
Yeoh, S.K. et al., 2015. On understanding the physics of the Enceladus south polar plume via numerical simulation. Icarus 253, 205–222.
Yin, A., 1989. Origin of regional, rooted low-angle normal faults: A mechanical model and its tectonic implications. Tectonics 8 (3), 469–482.
Yin, A., 2000. Mode of Cenozoic east–west extension in Tibet suggesting a common origin of rifts in Asia during the Indo-Asian collision. J. Geophys. Res.: Solid Earth (1978–2012) 105 (B9), 21745–21759.
Yin, A., 2010. Cenozoic tectonic evolution of Asia: A preliminary synthesis. Tectonophysics 488 (1), 293–325.
Yin, A., 2012a. Structural analysis of the Valles Marineris fault zone: Possible evidence for large-scale strike-slip faulting on Mars. Lithosphere 4 (4), 286–330.
Yin, A., 2012b. An episodic slab-rollback model for the origin of the Tharsis rise on Mars: Implications for initiation of local plate subduction and final unification of a kinematically linked global plate-tectonic network on Earth. Lithosphere 4 (6), 553–593.
Yin, A.N., Dunn, J.F., 1992. Structural and stratigraphic development of the Whipple-Chemehuevi detachment fault system, southeastern California: Implications for the geometrical evolution of domal and basinal low-angle normal faults. Geol. Soc. Am. Bull. 104 (6), 659–674.
Yin, A., Kelty, T.K., 1991. Structural evolution of the Lewis plate in Glacier National Park, Montana: Implications for regional tectonic development. Geol. Soc. Am. Bull. 103 (8), 1073–1089.
Yin, A., Taylor, M.H., 2011. Mechanics of V-shaped conjugate strike-slip faults and the corresponding continuum mode of continental deformation. Geol. Soc. Am. Bull. 123 (9–10), 1798–1821.
Yin, A. et al., 2002. Tectonic history of the Altyn Tagh fault system in northern Tibet inferred from Cenozoic sedimentation. Geol. Soc. Am. Bull. 114 (10), 1257–1295.
Yin, A. et al., 2008. Cenozoic tectonic evolution of the Qaidam basin and its surrounding regions (part 3): Structural geology, sedimentation, and regional tectonic reconstruction. Geol. Soc. Am. Bull. 120 (7–8), 847–876.